



HAL
open science

Strain patterns in glacitectonically thrust sediments and conditions during thrusting

Matthew J Warbritton, Neal R Iverson, France Lagroix, Anders Schomacker

► **To cite this version:**

Matthew J Warbritton, Neal R Iverson, France Lagroix, Anders Schomacker. Strain patterns in glacitectonically thrust sediments and conditions during thrusting. *Journal of Structural Geology*, 2020, 137, pp.104064. 10.1016/j.jsg.2020.104064 . hal-03033129

HAL Id: hal-03033129

<https://hal.science/hal-03033129>

Submitted on 7 Dec 2020

HAL is a multi-disciplinary open access archive for the deposit and dissemination of scientific research documents, whether they are published or not. The documents may come from teaching and research institutions in France or abroad, or from public or private research centers.

L'archive ouverte pluridisciplinaire **HAL**, est destinée au dépôt et à la diffusion de documents scientifiques de niveau recherche, publiés ou non, émanant des établissements d'enseignement et de recherche français ou étrangers, des laboratoires publics ou privés.

1
2
3 **Strain patterns in glacitectonically thrust sediments and**
4 **conditions during thrusting**
5

6 Matthew.J. WARBRITTON^a, Neal R. IVERSON^{a*}, France LAGROIX^b, and Anders
7 SCHOMACKER^c
8

9 ^aDepartment of Geological and Atmospheric Sciences, Iowa State University, 2237 Osborn Dr.,
10 Ames, IA 50011, USA

11 ^bInstitut de Physique du Globe de Paris, Sorbonne Paris Cité, Univ. Paris Diderot, UMR 7154
12 CNRS, 1 rue Jussieu, 75005 Paris, France

13 ^cDepartment of Geosciences, UiT—The Arctic University of Norway, Tromsø, Norway
14

15 *Corresponding author: Neal R. Iverson, Department of Geological and Atmospheric
16 Sciences, Iowa State University, 2237 Osborn Dr., Ames, IA 50011, USA

17 email: niverson@iastate.edu

18 t: 1 515 294 8048

19 Keywords: Glacitectonic deformation; Thrust sheets; Anisotropy of magnetic
20 susceptibility; Permafrost; Pore pressure
21
22

23 Strain patterns in glacitectonically thrust sediments and conditions during
24 thrusting

25 **Abstract**

26 Glacitectonically thrust blocks of unlithified sediment are commonly inferred to have been
27 frozen during thrusting, with implications for paleoclimate and glacier dynamics. We inferred
28 strain patterns within thrust blocks of glaciolacustrine mud in the Rubjerg Knude and Møns
29 Klint glacitectonic complexes of coastal Denmark to try to assess whether the mud was frozen
30 during thrusting. Fabrics based on the anisotropy of magnetic susceptibility (AMS) of the muds
31 are interpreted with results of ring-shear experiments and models of AMS fabric development
32 during layer-parallel shortening (LPS). In intact distal stratigraphy, fabrics indicate moderate
33 LPS. Fabrics where thrusts have disrupted more proximal stratigraphy indicate rotation of mud
34 sheets during thrusting with insufficient penetrative strain to reset the LPS fabric. The exception
35 is within decimeters of faults at Rubjerg Knude where shear overprinted the LPS fabric.
36 Although these data indicate that mud sheets were mostly rigid during thrusting, this is not
37 necessarily evidence of permafrost. Critical-taper theory indicates that even a gentle slope of the
38 proglacial surface away from the glacier margin would have allowed slip without internal
39 deformation of thrust sheets, requiring only minimal pore-water pressures.

40 **1. Introduction**

41 Glacitectonic thrust complexes with along-flow lengths of kilometers and depths of tens to a
42 few hundreds of meters (e.g., Pedersen, 2014; Phillips, 2018) are among the most spectacular of
43 glacial geologic structures. Interest in them derives from their geomorphic expression,
44 commonly as composite ridges that form end moraines or as the hills of hill-hole pairs (e.g.,
45 Aber and Ber, 2007). They are also of interest as analogs for orogenic belts (Croot, 1987;

46 Hudleston, 1992; Bennett, 2001; Van der Wateren, 2002; Phillips, 2018) and because of the short
47 periods over which they can form (Benediktsson et al., 2010). Environmental effects of thrust
48 complexes include their influence on subsurface water flow (e.g., Klint et al., 2013), on rates of
49 mass wasting and erosion of coastal cliffs (Pedersen and Møller, 2004; Kołodziejczyk et al.,
50 2018), and on site selection for future nuclear waste repositories (Talbot, 1999; Iverson and
51 Person, 2012).

52 Importantly, glacitectonic thrust complexes may also provide information about whether
53 climates at the margins of former glaciers were sufficiently cold to sustain permafrost. Thrust
54 complexes form beneath glacier margins and can extend in front of them more than 5 km in
55 exceptional cases (Aber and Ber, 2007). Although complexes sometimes contain thrust blocks
56 consisting of sedimentary rocks, some or all of thrust material is usually weaker, unlithified,
57 glacial sediment. As emphasized in reviews by Bennett (2001) and Van der Wateren (2002),
58 such sediments are commonly inferred to have been frozen during thrusting (e.g., Mathews and
59 Mackay, 1960; Moran et al., 1980; Thomas, 1984; Menzies, 1990; Mooers, 1990; Boulton et al.,
60 1999; Benn and Clapperton, 2000; Clayton et al., 2001; Burke et al., 2009).

61 Although proglacial thrusting can definitively occur in the absence of permafrost (e.g.,
62 Ingólfsson, 1988; Van der Wateren, 2002; Kuriger et al., 2006; Benediktsson et al., 2009), we
63 explore whether the distribution of strain in individual thrust blocks of complexes can be used to
64 test whether sediments were frozen during thrusting. Specifically, frozen sediments are expected
65 to be stronger (e.g., Moore, 2014) and less subject to ductile strain than unfrozen sediments (e.g.,
66 Feeser, 1988), particularly at temperatures well below the freezing point, at which weakening by
67 pre-melted water is minimal (Moore, 2014; Wang and Nishimura, 2017).

68 Herein we investigate strain patterns within the fine-grained sediments of selected thrust
69 sheets of two glacitectonic complexes of coastal Denmark: Rubjerg Knude and Møns Klint (e.g.,
70 Johnstrup, 1874, 1882; Jessen, 1899; Pedersen, 2014). Strain patterns are determined by
71 measuring the anisotropy of magnetic susceptibility (AMS) of the sediments. Determination of
72 the magnetic mineralogy, results of ring-shear experiments in which sediments were sheared, and
73 models of AMS fabric development in orogenic fold and thrust belts are used to interpret the
74 AMS data. We find that thrust blocks behaved too rigidly to reset fabrics during thrusting, except
75 within decimeters of bounding thrust surfaces. Considering shear stresses on thrust faults
76 indicates, however, that a combination of positive pore-water pressure and a proglacial surface
77 sloping down-flow above thrusts can cause thrusting of rigid slabs without added shearing
78 resistance provided by pore ice.

79 **2. Field settings**

80 The Rubjerg Knude and Møns Klint glacitectonic complexes of Denmark consist of
81 décollement surfaces that dip gently up-glacier, as inferred from reconstructions based on
82 exposed stratigraphy and structures and isostatic depression by ice (Pederson, 2005; Pedersen
83 and Gravesen, 2009). The décollements are overlain by thrust faults consisting of ramps and
84 flats and associated anticlines and synclines. Both complexes formed in front of the advancing
85 margin of the Scandinavian Ice Sheet (e.g., Houmark-Nielsen & Kjær, 2003; Pedersen, 2014)
86 and are structurally similar to thrust and folded orogenic belts. These complexes lie in the
87 region that Sollid and Sorbel (1988) thought was a sub-freezing marginal zone of the ice sheet,
88 based on relict ice-cored moraines and ice-wedge polygons.

89

90

91 *2.1. Rubjerg Knude*

92 The Rubjerg Knude complex, first recognized by Johnstrup (1874, 1882) and studied in
93 detail by Pedersen (2005), is located in northwestern Denmark along the northwest coast of
94 Jutland (Fig. 1). The complex is well exposed for 6 km along a coastal cliff that is 60 m above
95 sea level at its highest point. The complex consists entirely of Weichselian or younger deposits,
96 including marine mud, glaciolacustrine mud, glaciofluvial sand and gravel, and till.

97 Of interest here, with decreasing age, are the Stortorn Formation (SF), Lønstrup Klint
98 Formation (LKF), and Rubjerg Knude Formation (RKF). The SF consists of predominantly clay
99 of the Older Yoldia Sea of the Middle Weichselian (Jensen, 1993). The sea existed until about 32
100 ka BP (Seidenkrantz and Knudsen, 1993) when the outlet to the North Sea was blocked by the
101 Norwegian Channel Ice Stream. This created an ice-dammed lake that persisted from ~32 to 29
102 ka BP (Sadolin et al., 1997; Houmark-Nielsen, 1999) and deposited the glaciolacustrine mud that
103 dominates the LKF. Close to 29 ka BP, the lake drained catastrophically, resulting in an
104 unconformity between the LKF and overlying glaciofluvial sand and gravel of the RKF (Sadolin
105 et al., 1997). At ~29 ka BP, during deposition of the RKF, the Kattegat Ice Stream (Houmark-
106 Nielsen, 2008), advanced south-southeast across the northern tip of Jutland (Fig. 1), initiating
107 deformation at Rubjerg Knude along a décollement ~40 m below sea level in the marine clay of
108 the SF (Pedersen, 2005). Faulting and folding extended 12 km in front of the glacier margin and
109 resulted in average shortening of 50%; thrust faults generally dip more steeply in the northern
110 and central areas where the décollement is deepest (Fig. 2A) (Pedersen, 2005).

111 In this study we focus on a distal section of the complex, called Ulstrup (Pedersen, 2005),
112 and a central section called Grønne Rende, with steeply dipping thrust sheets (Fig 2). The
113 Ulstrup section consists of predominantly horizontal layers of the LKF overlying the RKF. The

114 section was considered to be undeformed until Pedersen (2005) found evidence for a horizontal
115 décollement at the southern end of the section along which the flat-lying sediment layers have
116 been displaced ~500 m. Otherwise the stratigraphy in this distal part of the complex is mostly
117 intact. In contrast, the Grønne Rende section consists of 13 steeply-dipping, and in some cases
118 near-vertical, thrust sheets. The LKF forms the most conspicuous sheets (Fig. 3), owing to the
119 ability of its mud to support vertical exposures. The sand and gravel of the RKF is interpreted to
120 have been syntectonically deposited in between and on top of thrust sheets during progressive
121 faulting and sheet rotation during longitudinal shortening (Pedersen, 2005). The average
122 displacement along these faults is 70 m (Pedersen, 2005).

123 Small-scale structures may provide insight into the formation of the complex. Ball-and-
124 pillow structures within the LKF may indicate where rapid loading caused pore-water pressure to
125 increase, leading to local diapir-like deformation of bedding surfaces (Lowe, 1975). Frost
126 wedges observed by Pedersen (2005) in the RKF near the paleo-ground surface indicate that
127 some frozen sediments were present during deformation. Also present in the RKF and perhaps
128 indicative of frozen sediments are kilelags (Pedersen, 2005), fissures that have opened during
129 initial brittle deformation and are filled with water-transported, syntectonically-deposited sand
130 (Sjørring, 1977).

131 2.2. *Møns Klint*

132 Møns Klint, in southeastern Denmark at Høje Møn (Fig. 1), has been a foundational location
133 for study of glacitectonics (e.g., Puggaard, 1851; Aber, 1980, 1982; Aber and Ber, 2007). The
134 exposure, in coastal cliffs that reach heights of 130 m and span 4 km, consists of Upper
135 Cretaceous chalk thrust over Weichselian sediments (Fig. 4). The sedimentary succession
136 includes the Ristinge Klint Till deposited ~60 ka BP by the Baltic ice advance from the

137 southeast, glaciolacustrine mud deposited after the recession of the Baltic ice, and till deposited
138 25-18 ka BP by ice advances from the northeast and glaciofluvial sand (Houmark-Nielsen, 1987;
139 Pedersen and Gravesen, 2009).

140 The initial deformation at Møns Klint commenced during the advance of the Young Baltic
141 Ice Stream from the south-southeast at ~18 ka BP (Houmark-Nielson and Kjær, 2003).
142 Deformation occurred along a décollement 80-100 m below sea level (Pedersen and Gravesen,
143 2009) and extended approximately 9 km in front of the advancing glacier. A later ice advance
144 from the northeast out of Sweden (16-17 ka) (Houmark-Nielsen, 2007) superimposed
145 deformation onto the eastern edge of the northern part of the complex from Slotsgavlene to
146 Maglevandsfald (Fig. 4) (Pedersen and Gravesen, 2009). The southernmost expression of the
147 superimposed deformation is near Maglevandsfald where a till wedge within chalk is folded
148 along an axis trending NW-SE (Pedersen and Gravesen, 2009). Farther south in the proximal part
149 of the complex (Pedersen, 2000), there is no evidence of the advance from the northeast, with
150 thrust faults striking approximately perpendicular to the Baltic Ice Stream advance from the
151 south-southeast (Fig. 4).

152 **3. Methods**

153 We use AMS, as a proxy for particle alignment, to interpret strain patterns in thrust blocks.
154 This method has been applied to tills deformed subglacially, using ring-shear experiments to
155 calibrate AMS to strain magnitude and direction (Thomason and Iverson, 2009; Shumway and
156 Iverson, 2009, Vreeland et al., 2015, McCracken et al., 2016; Ives and Iverson, 2019), and
157 applied to glacier ice with debris (Fleming et al., 2013a) and to sediments with glaciotectionic
158 structures (Fleming et al., 2013b). Using AMS in glacial sediments requires collecting multiple,
159 closely-spaced, intact sediment specimens, so a fabric representative of the sampled region can

160 be determined. Tests to determine magnetic mineralogy of the sediments (Appendix) and a ring-
161 shear experiment on mud from Rubjerg Knude also contribute to our interpretations.

162

163 *3.1. AMS Sampling*

164 To collect samples a planar face is created by scrapping an exposure sufficiently to expose
165 undisturbed sediment. Aluminum, 18 mm, cubic boxes, open on two ends, are inserted in the
166 face in as tight a grid as was possible without disturbing adjacent boxes (Fig. 5), with 18-25
167 samples used to determine a fabric. Plastic boxes usually used for such sampling (e.g.,
168 McCracken et al., 2016) are too weak to be pressed into the hard, consolidated muds of
169 glacitectonic complexes. After measuring the orientation and position of each box, it is
170 excavated, with excess mud trimmed from the open ends of the box with a wire saw. With a
171 plunger the mud is extruded into a plastic box of the same size and the box capped, labelled, and
172 sealed in plastic to inhibit moisture loss. In a few cases sandier layers can be sampled by pushing
173 plastic boxes into the sediment directly.

174 At Rubjerg Knude, sampling was focused on thrust sheets in the Grønne Rende section (Fig.
175 2B), but additional samples were collected within the mostly intact stratigraphy of the distal
176 Ulstrup section (Fig. 2C). The distal end of the complex was chosen for sampling to determine
177 strain patterns in the absence of pervasive thrusting, so the effects of thrusting on strain in the
178 Grønne Rende section could be isolated. Samples at both sections were mainly from the
179 glaciolacustrine mud of the LKF because its cohesion allowed the collection of minimally
180 disturbed samples, unlike the friable sand of the RKF. At Ulstrup, flat-lying mud (striking 273°,
181 dipping 3° south) of the LKF (Fig. 2B) was sampled along two vertical transects (three fabrics
182 per transect), beneath the unconformity with the RKF.

183 At Grønne Rende the primary objective was to sample thrust blocks along transects normal to
184 fault surfaces. Three thrust sheets (GR10, GR07, and GR05, Fig. 2a) with conspicuous, near-
185 vertical exposures of the LKF were chosen for study based largely on their accessibility and
186 safety concerns. These sheets have strikes of 266-285° in agreement with thrusting driven by the
187 Kattegat Ice Stream advancing from the north and dips of 56° N to near vertical. Also accessible
188 at GR10 and GR07 were dip-slopes of the LKF eroded into the cliff-face by mass wasting
189 processes along bedding planes, so these surfaces were also sampled, taking care in all cases to
190 measure the orientation of samples.

191 Our principal concern is how strain varied with distance from the surfaces of thrust faults, so
192 through-going fault surfaces needed to be identified. At Rubjerg Knude we used slickensides that
193 result from P shears and Riedel shears that grow and intersect during slip, forming asymmetric
194 steps on fault surfaces (Petit, 1987; Doblas, 1998) near the base of the LKF (Fig. 6). In thrust
195 sheets GR10 and GR05, slickensides could at some locations be identified and were used to
196 reference fault-normal transects of AMS samples (Fig. 7A, B). No slickensides were found at
197 thrust sheet GR07. Although some samples for AMS fabrics were gathered in thrust sheets in the
198 absence of adjacent slickensides (Warbritton, 2019), we report data from fault-normal transects
199 only where slickensides provided an indicator of thrust position (13 fabrics). We also consider
200 AMS fabrics collected from two eroded dip-slopes (6 fabrics) distant from thrust faults.

201 At Møns Klint, glaciolacustrine mud of the Middle Weichselian in the proximal part of the
202 complex (Fig. 4), overlain along a sharp, gently dipping contact by Maastrichtian chalk (Fig. 5),
203 was sampled along a 4 m long section (Fig. 8). The fault between the chalk and mud strikes 79°
204 ($\pm 7^\circ$) and dips 18° ($\pm 4^\circ$), consistent with thrusting driven by the Young Baltic ice stream
205 advance from south-southeast (Pederson and Gravesen, 2009). Samples were gathered in four

206 adjacent vertical transects, 0.9-2.0 m high, referenced to the contact and sufficient for 17 AMS
207 fabrics.

208 3.2. AMS analysis

209 AMS was measured with a KLY-3S Kappabridge at the University of Wisconsin-Madison.
210 This device subjects a sample to a magnetic field of constant strength, H , in 15 different
211 orientations. The intensity of magnetization, M , is defined as kH , where k is the susceptibility
212 (Jelínek, 1978; Tarling and Hrouda, 1993). In three dimensions, the susceptibility is described
213 with a second-rank tensor, and the principal susceptibilities of this tensor, k_1 , k_2 , and k_3 , are
214 represented as the long, intermediate, and short axes, respectively, of an ellipsoid. In materials
215 that are anisotropic, the susceptibility varies with sample orientation. For non-equant magnetic
216 grains that are multi-domain or pseudo-single-domain and have shape anisotropy, such as
217 magnetite, the susceptibility is strongest parallel to the long axes of grains (Tarling and Hrouda,
218 1993). Deformation of sediment preferentially aligns grains and creates AMS. As described in
219 the Appendix, mineral magnetic analyses were conducted at the *Institut de Physique du Globe de*
220 *Paris* to determine the mineralogy and magnetic grain size of the dominant AMS carrier of the
221 muds from the two complexes.

222 If the orientations of principal susceptibilities are measured for each of multiple till samples,
223 they together define a fabric that helps indicate the magnitude and orientation of strain (Hooyer
224 et al., 2008). The orientations of maximum clustering of k_1 , k_2 , and k_3 are each characterized with
225 a V_1 eigenvector, and the strength of the preferred orientation about V_1 is characterized with an S_1
226 eigenvalue (Mark, 1973). We thus analyze orientations of principal susceptibilities separately,
227 rather than using tensor statistics. For poorly clustered data, our technique can lead to V_1
228 eigenvectors for k_1 , k_2 , and k_3 orientations that are not orthogonal. However, principal

229 susceptibility orientations from our field samples are well-clustered, so we elect to follow the
230 tradition in glacial geology of using eigenvectors and eigenvalues to characterize fabrics. $S_1 = 1.0$
231 indicates perfect alignment and $S_1 = 0.33$ indicates an isotropic distribution (i.e., no alignment).
232 Orientation data are plotted in lower hemisphere, equal-area stereonet. Importantly, in
233 stereonet displaying fabrics from dipping thrust sheets, the plane of the primitive circle is taken
234 to be the attitude of the thrust sheet, as indicated by the orientations of thrust faults adjacent to
235 sampling locations or as indicated by bedding attitude in the case of samples from dip-slopes.
236 This allows easier comparison with experimental and field data in which shear or bedding is
237 horizontal. At sections studied where both fault and bedding attitudes could be measured, they
238 tended to be nearly the same ($< 3^\circ$ differences in strike and dip), although elsewhere at Rubjerg
239 Knude that is not necessarily true (Pederson, 2005). In the massive mud sampled at Møns Klint,
240 no bedding could be identified.

241 *3.3. Ring-shear experiment*

242 To help establish the relationship between shear strain orientation and the AMS signature, an
243 experiment with a ring-shear device was conducted with mud of the LKF. The device (Iverson et
244 al., 1997) has been used extensively to shear subglacial till with the same objective (Hooyer et
245 al., 2008; Shumway and Iverson, 2009; Vreeland et al., 2015; McCracken et al., 2016; Ives and
246 Iverson, 2019). Sediment with its pore water drained to atmospheric pressure is sheared within a
247 ring-shaped chamber (O.D.= 0.6 m, width = 0.115 m) between horizontal platens. The upper
248 platen, which can move up or down as sediment porosity changes, applies a steady stress normal
249 to the shear plane. During shear, the lower platen and lateral walls of the lower half of the sample
250 chamber rotate at a constant speed. Shearing occurs in a zone, < 35 mm thick, centered on the
251 break between the rotating lower walls and static upper walls.

252 The LKF mud was first vigorously mixed with distilled water so aggregates would break
253 down and grain orientations would be randomized. The mixture was then added to the sample
254 chamber as a slurry to a thickness of 0.06 m. A normal stress (65 kPa) was applied for a period
255 of 11 days to consolidate the mud. The amount of consolidation (14.5%) was determined by
256 using two dial gauges to measure the downward movement of the upper platen, which resulted
257 from the decrease in specimen thickness. The test was then run at a constant shear rate of $1.27 \times$
258 10^{-5} m/s to a displacement of 0.6 m along the sample centerline. After the test was completed, 53
259 samples were collected for AMS analysis. A smooth, flat surface was exposed just below the
260 uppermost extent of the shear zone, as inferred from past experiments on tills (Hooyer et al.,
261 2008), and samples were collected by pressing into the mud plastic boxes like those used for the
262 field measurements.

263 4. Results

264 4.1. Experiments

265 Tests aimed at assessing magnetic mineralogy indicate that the dominant carrier of magnetic
266 susceptibility of the glaciolacustrine muds from the two thrust complexes is multi-domain or
267 pseudo-single domain magnetite (Appendix). Such magnetite has normal shape anisotropy
268 (Tarling and Hrouda, 1993), so the orientations of principal susceptibilities should reflect grain
269 orientation.

270 This expectation is confirmed at Rubjerg Knude by the ring-shear experiment conducted on
271 the mud sampled there (Fig. 9A). The V_1 orientation based on 53 k_1 orientations indeed parallels
272 the shearing direction and plunges “up-glacier” 11° , consistent with past ring-shear experiments
273 on AMS of tills with magnetite as the dominant carrier mineral, including tills derived from
274 remobilized lake sediments (Fig. 9B) (Hooyer et al., 2008; Thomason & Iverson, 2009; Vreeland

275 et al., 2015; Ives and Iverson, 2019). Also consistent with past experiments are the orientations
276 of V_1 for k_2 and k_3 : k_2 orientations are horizontal and perpendicular to shear, and k_3 orientations
277 plunge steeply ($\sim 80^\circ$) “down-glacier.” However, unlike past results of experiments on tills,
278 including on those consisting of remobilized lake sediments (Fig. 9B), clustering of k_1 and k_2
279 orientations is weak, with $S_1 = 0.59$ in each case as opposed to $S_1 > 0.9$ for fine-grained till
280 (Hooyer et al., 2008). Rather than clustering strongly, these principal susceptibilities form
281 asymmetric girdles that dip gently “up-glacier” (Fig. 9A).

282 Unlike many studies of the magnetism of deformed rocks, we do not use various indices of
283 the magnitude of anisotropy of individual samples to infer strain; ring-shear experiments
284 conducted to wide a range of strains on tills that contain magnetite as the source of AMS show
285 no systematic dependence of these indices on strain magnitude (Hooyer and Iverson, 2008;
286 Vreeland et al., 2015).

287 4.2. *Rubjerg Knude*

288 Principal-susceptibility orientations for the six fabrics from the distal end of the Rubjerg
289 Knude thrust complex (Ulstrup section) display a relatively uniform pattern (Fig. 10). Here, the
290 mud and overlying sand units are horizontal and with little macroscopic evidence of deformation.
291 A stereonet combining principal-susceptibility orientations from these fabrics (Fig. 11A)
292 demonstrates strong clustering of the three principal susceptibilities ($S_1 \geq 0.81$). Orientations of
293 k_1 cluster near perpendicular to the glacier flow direction (south-southwest, Pedersen, 2005), k_2
294 orientations are close to horizontal and parallel to the flow direction, and k_3 orientations plunge
295 near vertically.

296 In thrust sheets of the Grønne Rende section, four fabric transects, one in GR10 and three in
297 GR05, were measured normal to bounding thrust faults with well-exposed fault slickensides (Fig.

298 12, 13). In all cases, orientations of principal susceptibilities are clustered ($S_1 \geq 0.77$). However,
299 two distinct fabric patterns are evident depending upon distance from the fault. Within 0.1 m and
300 ~ 0.7 m of the GR10 and GR05 fault surfaces, respectively, orientations of principal
301 susceptibilities are similar to those of ring-shear experiments (Fig. 9), if data are plotted relative
302 to the attitude of the fault surfaces. If all data from close to faults are combined in a single such
303 stereoplot, the similarity is clearest (Fig. 11B, compare with Fig. 9A, B): the V_1 of k_1 orientations
304 is roughly parallel to the glacier flow direction (SSW) and plunges gently up-glacier relative to
305 the plane of the fault. Orientations of k_2 cluster perpendicular to the shear direction. Orientations
306 of k_3 are clustered the strongest ($S_1 = 0.92$) and steeply plunge down-glacier relative to the plane
307 of the fault. A difference between the field and ring-shear AMS data is that k_2 and k_3 clusters are
308 rotated $\sim 10^\circ$ around the axis of the k_1 cluster

309 In contrast, farther away from faults, orientations of principal susceptibilities cluster similarly
310 to fabrics from the distal part of the thrust complex at Ulstrup (Fig. 11C, compare with Fig.
311 11A): k_1 orientations cluster in the fault plane and sub-perpendicular to the flow direction; k_2
312 orientations also cluster in the fault plane but sub-parallel to the flow direction. Orientations of k_3
313 cluster normal to the fault surface. Unlike fabrics from Ulstrup, k_1 and k_2 clusters are rotated
314 counterclockwise 27° from being perpendicular and parallel to the regional glacier flow
315 direction, respectively. Possibly significant, however, is that five of the seven fabrics used to
316 compile Figure 11C are from thrust sheet GR05, which strikes in a direction consistent with a
317 local thrusting direction that is similarly rotated (Fig. 13).

318 All fabrics from samples collected from eroded dip-slope surfaces away from faults and
319 plotted on stereonets relative to the dip of the bedding also have AMS fabrics similar to those at
320 the distal end of the thrust complex. Combining the susceptibility orientations from these fabrics

321 on one stereonet shows this clearly (Fig. 11D, compare with Fig. 11A). Orientations of k_1 cluster
322 near perpendicular to the glacier flow direction; k_2 orientations cluster in the plane of the bedding
323 and parallel to the flow direction, and k_3 orientations cluster parallel to the glacier flow direction
324 and plunge near-normal to bedding. A slight difference is that k_2 and k_3 clusters from dip-slope
325 fabrics indicate they dip up-glacier relative to bedding, approximately 15° .

326 *4.3. Møns Klint*

327 Fabrics from the exposure at Møns Klint, if plotted on stereonets relative to the plane of the
328 fault and grouped according to their distance from it (Fig. 14), are similar to some fabrics at
329 Rubjerg Knude. Orientations of k_1 cluster either roughly perpendicular to the glacier-flow
330 direction (NNW, as inferred by Pedersen and Gravesen (2009) from the strikes of thrust faults in
331 the complex) or at an angle less than $\sim 45^\circ$ to the flow direction. Orientations of k_3 tend to cluster
332 with steep plunges up-glacier; k_2 orientations are the most weakly clustered but tend either to
333 plunge slightly down-glacier, where k_1 clusters are perpendicular to flow (Fig. 14, < 0.36 m,
334 1.19-1.8 m), or to trend at an angle greater than $\sim 50^\circ$ to the flow direction where k_1 clusters are
335 more closely aligned with the flow direction (Fig. 14, 0.51-0.98 m). The former fabrics are
336 similar to those of the intact distal stratigraphy of the Rubjerg Knude complex (Fig. 11A), as
337 well as parts of thrust sheets in that complex away from faults (Fig. 11C, D).

338 **5. Discussion**

339 *5.1. AMS fabric interpretation*

340 In addition to our results indicating that the AMS of the thrust sheets is controlled by multi-
341 domain or pseudo-single domain magnetite (Appendix), we have two means of interpreting AMS
342 fabrics. Results from ring-shear experiments on the LKF mud and on tills provide a model for
343 AMS development in till deformed predominately in simple shear. In addition, models of AMS

344 fabric development in larger-scale compressional tectonic environments, tested experimentally,
345 provide guidance for interpreting fabric development during layer-parallel shortening.

346 Experimental shearing of the LKF mud yields V_1 eigenvectors for the three principal
347 susceptibilities that are similar to those obtained in identical experiments conducted on fine-
348 grained tills in which magnetite was the dominant magnetic mineral (Fig. 9). Eigenvectors based
349 on k_1 orientations are close to the shearing direction (within 11°) and plunge gently up-glacier;
350 those based on k_2 orientations are nearly perpendicular to the shearing direction (within 7°) in the
351 plane of the fault, and those based on k_3 plunge steeply down-glacier.

352 Dissimilar, however, is that in the experiment on mud, k_1 and k_2 orientations did not cluster
353 but formed asymmetric girdles (Fig. 9A), despite shearing displacements that were just as large
354 as in the till experiments. The lack of clustering of k_1 and k_2 orientations likely reflects strain
355 localization in the mud in thin shear bands, a characteristic behavior of clay-rich soils in
356 geotechnical experiments in which strain commonly localizes in zones 0.3-10 mm thick
357 (Morgenstern and Tchalenko, 1967; Hicher et al., 1994). AMS samples, in contrast, were
358 collected after the experiment over a mud thickness of 16 mm (the sampling box dimension),
359 which would have resulted in the collection of significant volumes of unsheared mud. This
360 unsheared mud, owing to its consolidation prior to the experiment and associated rotation of
361 particles toward the horizontal, would have had a k_1 - k_2 girdle in the plane of shear and a vertical
362 cluster of k_3 orientations (e.g., Tarling and Hrouda, 1993; Parés, 2015). The asymmetric k_1 - k_2
363 girdle that is observed, therefore, likely reflects a significant volume of unsheared mud in the
364 AMS samples. Thus, although eigenvectors from the mud experiment are fully consistent with
365 those developed from simple shear of tills, clustering of k_1 and k_2 orientations from experiments
366 with fine-grained till probably better reflects the AMS response of the mud to simple shear, as

367 long as thicknesses of shear zones sampled in the field exceeded the thickness of sample boxes.
368 We conclude, therefore, that the clustered orientations of principal susceptibilities obtained in
369 ring-shear experiments on tills, formed subglacially through remobilization of glaciolacustrine
370 mud and with their AMS controlled by magnetite (Fig. 9b), is an appropriate model for the muds
371 of this study, if they have been subjected to a sufficient strain.

372 On that basis, a solid conclusion is that the fabric pattern close to thrust faults ($< \sim 0.7$ m) at
373 Rubjerg Knude (Fig. 11b) reflects shear of the mud during thrusting. Shear must have been to a
374 sufficiently high strain close to faults to fully overprint the AMS fabric that existed prior to
375 thrusting. At Møns Klint, on the other hand, despite collection of AMS samples as close as 3 cm
376 to the fault between the chalk and underlying mud, this fabric pattern indicative of simple shear
377 is absent.

378 Additional insights into the fabric patterns at Rubjerg Knude and Møns Klint come from
379 studies of AMS fabric development in deformed rocks (see Borradaile and Henry, 1997; Parés,
380 2015, for reviews) and sediments (e.g., Collombat et al., 1995; Housen and Kanamatsu 2003;
381 Caricchi et al., 2016) in crustal tectonic environments. A leading model developed from such
382 field studies (notably by Averbuch et al., 1992; Borradaile and Henry, 1997; Bakhtari et al.,
383 1998; Saint-Bezar et al., 2002) and more recently tested in analogue sandbox experiments
384 (Almqvist and Koyi, 2018) allows interpretation of fabrics resulting from layer-parallel
385 shortening (LPS) in fold and thrust belts and accretionary prisms. The model (Fig. 15) describes
386 the change in AMS fabric pattern from a depositional fabric, found in forefield regions, to fabrics
387 indicative of progressively higher-strain LPS towards the hinterland. The depositional fabric,
388 with k_3 orientations clustering vertically and k_1 and k_2 orientations in a horizontal girdle (fabric 1
389 of Fig. 15), reflects the horizontal settling and subsequent consolidation during burial of oblate,

390 clay-sized particles (Tarling and Hrouda, 1993). Common in fold-thrust environments are
391 intermediate fabrics in which this depositional fabric has been overprinted by a small amount of
392 LPS. This fabric (fabric 2 of Fig. 15) reflects consolidation greater than LPS, such that k_3
393 orientations remain vertical. Orientations of k_1 , however, rotate into the direction of maximum
394 extension, which is horizontal and perpendicular to the shortening direction. With still more LPS,
395 a vertical k_2 - k_3 girdle forms parallel to shortening (fabric 3), which transitions at still greater
396 strain to k_2 and k_3 clusters that are vertical and parallel to the shortening direction, respectively
397 (fabric 4). This highest-strain AMS fabric has been measured in till interpreted to have been
398 extruded upward into basal crevasses (Ankerstjerne et al., 2015).

399 AMS fabrics measured at Rubjerg Knude in the distal Ulstrup section and away from thrusts
400 in the Grønne Rende section, as well as most fabrics measured at Møns Klint, are similar to
401 fabric 2 of this model. Orientations of k_1 cluster in the plane of the bedding or fault and
402 perpendicular or sub-perpendicular to the thrusting direction; k_2 orientations also cluster in the
403 plane of the fault or bedding but are parallel or sub-parallel to thrusting, and k_3 orientations either
404 cluster vertically or are steeply dipping. Therefore, prior to thrusting of mud sheets at Rubjerg
405 Knude and Møns Klint the mud was consolidated (fabric 1, Fig. 15) and underwent minor
406 shortening parallel to bedding. More importantly, thrusting did not change this fabric at Grønne
407 Rende, except within decimeters of fault surfaces where simple shear reset the LPS fabrics. At
408 Møns Klint, there is no evidence of thrusting resetting this fabric, likely indicating that shear was
409 focused in the ~3 cm of mud closest to the fault where the mud was not sampled (Figs. 5 and 14).
410 AMS of sediments across basal décollements of accretionary prisms sometimes indicate a similar
411 lack of detectable overprinting by shear deformation (Housen et al., 1996). In contrast, the
412 superimposed deformation onto the eastern edge of the northern part of the complex from

413 Slotsgavlene to Maglevandsfald (Fig. 4), which occurred later, recumbently folded the glacial
414 sediments (Pedersen and Gravesen, 2009), likely resetting LPS fabrics.

415 The clear implication is that during thrusting sheets were rotated, with little internal
416 deformation except very near faults. As noted, a leading hypothesis for glacitectonic thrusting of
417 rigid sheets of unlithified sediment is that permafrost made thrusting of coherent sheets possible
418 through some combination of increasing their strengths and serving as a barrier for groundwater
419 flow. In that case, the narrow zones of shear near thrust surfaces might be interpreted as the
420 result of heat dissipation during slip and the associated warming or melting of pore ice there.
421 Warbritton (2019) showed that heat dissipation from the average displacement on faults at
422 Rubjerg Knude estimated by Pedersen (2005, ~70 m) was sufficient to warm permafrost
423 substantially near slip surfaces. Potentially this softened the permafrost through production of
424 pre-melted water, enabled strain localized in narrow zones, and reduced shear stresses
425 sufficiently to allow the slip of mostly intact sheets.

426 *5.2. Thrusting of intact sheets without permafrost*

427 We now step back and consider more generally whether thrusting of largely intact sediment
428 sheets can occur under fully thawed conditions, by appealing to the effects of pore-water
429 pressure and thrust geometry rather than to permafrost. Consider a thrust sheet (Fig. 16) with the
430 wedge geometry commonly considered in studies of crustal faulting (e.g., Turcotte and Schubert,
431 2014). Wedge-shaped thrust sheets were also considered by Pedersen (2005) in his
432 reconstructions of thrusting at Rubjerg Knude. The upper surface of the thrust wedge slopes at
433 an angle, α , toward the distal end of the wedge, as expected if layer-parallel shortening is largest
434 near the glacier margin and is accompanied perhaps by proximal thrusting in the wedge. The
435 thrust ramp dips in the opposite direction at an angle, β . The thickness of the wedge, H , is

436 defined normal to the thrust surface. The wedge is pushed from upstream along the x coordinate,
437 defined parallel to the thrust ramp, by a force that reflects the depth integral of the stress, σ_x (Fig.
438 16). In the opposite direction is a shear stress, τ_b , acting along the base of the thrust ramp.

439 In their study of the mechanics of fold and thrust belts, Davis et al. (1983) balanced forces on
440 the wedge and considered the stresses required for its Coulomb failure to estimate τ_b for the
441 special case of a wedge deforming internally at its Coulomb strength. In that case, shear failure
442 occurs under a traction, $S = S_0 + \mu (\sigma_z - p_w)$, where S_0 is the sediment cohesion, σ_z is the total
443 stress, p_w is the pore-water pressure, and μ is an internal friction coefficient commonly expressed
444 in terms of a friction angle φ such that $\mu = \tan \varphi$. For the small values of α and β relevant to
445 this problem, for which $\sin \alpha \approx \alpha$ and $\sin \beta \approx \beta$, and assuming the wedge is saturated with water
446 everywhere, Davis et al. (1983) derived the shear stress on the thrust fault required to deform the
447 wedge:

$$448 \quad \tau_b = (\rho - \rho_w)gH\alpha + (1 - \lambda)K\rho gH(\alpha + \beta), \quad (1)$$

449 where ρ is the density of the sediment grains of the wedge, and ρ_w is the density of pore water.

450 Two dimensionless quantities are particularly important in Eq. (1): the water pressure ratio,
451 $\lambda = p_w / \sigma_z$ and the parameter, K , which scales with the frictional strength of the wedge. The shear
452 stress at the base must balance the down-slope component of gravity acting on the sloping
453 surface of the wedge, as given by the first right-hand term, and must also balance the force on the
454 upstream end of the wedge as limited by the wedge's Coulomb strength and given by the second
455 right-hand term. In deriving Eq. (1), Davis et al. (1983) assumed zero cohesion in the wedge, so
456 for the fine-grained and likely cohesive muds of this study, Eq. (1) provides a minimum value of
457 the stress required to deform the wedge.

458 For the wedge to slip along its basal fault without deforming the wedge internally, the
 459 frictional stress resisting slip, S_b , at the base of the wedge must be less than τ_b . Defining μ_b and
 460 λ_b as the friction coefficient and water pressure ratio, respectively, at the base of the wedge,

$$461 \quad S_b = \mu_b(1 - \lambda_b)\rho gH. \quad (2)$$

462 Thus, the condition for slip without internal deformation of the wedge is

$$463 \quad \mu_b(1 - \lambda_b)\rho gH < (\rho - \rho_w)gH\alpha + (1 - \lambda)K\rho gH(\alpha + \beta). \quad (3)$$

464 To maximize slip resistance on the fault and to thereby optimize the potential for deforming a
 465 wedge of a given geometry and strength, we assume that $\lambda_b = \lambda$, despite the possibility that pore-
 466 water pressure might be elevated along the fault relative to the wedge overall. Assuming $\lambda_b = \lambda$,
 467 and rearranging Eq. (3) yields the pore-pressure condition required for slip without internal
 468 deformation of the wedge:

$$469 \quad \lambda > 1 - \frac{\alpha(1 - \frac{\rho_w}{\rho})}{\mu_b - K(\alpha + \beta)}. \quad (4)$$

470 Despite the possibility that sliding friction was less than internal friction, we set the friction
 471 coefficient of the fault equal to the internal friction coefficient of the wedge, $\mu_b = \mu = \tan \varphi$, to
 472 further optimize the potential for deforming it. In that case, as shown by Davis et al. (1983), a
 473 good approximation for the Coulomb strength factor is

$$474 \quad K = \frac{\sin \varphi}{1 - \sin \varphi} + \frac{\sin^2 \varphi}{\cos^2 \varphi}. \quad (5)$$

475 Eqs. (4) and (5) illustrate that if the glacier forefield sloped down-glacier at even a small
 476 angle α , a wide a range of pore-pressure ratios could have resulted in thrusting without internal
 477 deformation of the thrust sheet. Fields of λ and α above and to the right of the plots of Figure 17
 478 indicate thrusting without internal deformation. For the thrust-ramp inclination that characterized
 479 initial thrusting in the Grønne Rende section at Rubjerg Knude (18°, Pedersen, 2005, p. 118),

480 even hydrostatic pore-water pressure (i.e., no upward groundwater flow) could have resulted in
481 fault slip without internal deformation, as long as $\alpha > 4.3^\circ$. Still smaller surface slopes would
482 have been required for later stages of faulting at Grønne Rende when thrust ramps became
483 steeper than 30° (Pedersen, 2005). Also, given that upward groundwater flow is common in
484 glacier forefields (e.g., Boulton and Caban, 1995), pore pressures could have easily exceeded
485 hydrostatic. Assumptions made in the derivation of Eqs. (4) and (5) (i.e., no internal cohesion, λ_b
486 $=\lambda$, and $\mu_b = \mu = \tan \varphi$) also make the estimates of λ and α in Figure 17 required for thrusting
487 without internal deformation conservatively large.

488 Unfortunately values of α are poorly known during thrusting at Grønne Rende. Pedersen's
489 (2005, p. 159) reconstruction indicates $\alpha > 5^\circ$ late during thrusting, but he argued that at the
490 beginning of thrusting the hinterland of the complex sloped toward the glacier 2° , owing to
491 isostatic depression by the glacier. Uncertainty in the value of α and its evolution during
492 thrusting clearly limit mechanical interpretations.

493 Nevertheless, at Rubjerg Knude and Møns Klint, during phases of thrusting when the
494 proglacial surface sloped away from the glacier, positive pore-water pressure could have caused
495 thrusting of intact sheets of mud in the absence of proglacial permafrost. This interpretation is
496 consistent with the field observations of Pedersen (2005), who interpreted sand-filled cracks,
497 local brecciation, and small-scale mud diapirism at Rubjerg Knude as reflecting high pore-water
498 pressures. It is also consistent with real-time observations of proglacial thrusting of smaller
499 sheets of unfrozen sediments by modern glaciers with little internal deformation of thrust sheets
500 (e.g., Kuriger et al., 2006).

501 Our calculations do not rule out that parts of thrust sheets may have been frozen (Pedersen,
502 2005) but support the viewpoint that permafrost is commonly not necessary for thrusting of

503 coherent sheets (e.g., Van der Wateren, 2002). The observation that shear at Rubjerg Knude
504 occurred only near thrust faults may indicate that in mud immediately adjacent to them the
505 condition $\lambda_b > \lambda$ was met—a reasonable expectation if consolidated mud of the LKF served as a
506 confining unit for groundwater flow.

507 **6. Conclusions**

508 Although AMS had been applied to sediments where macroscopic structures indicate
509 glaciotectonic deformation (Fleming et al., 2013b), this study is the first attempt to apply AMS to
510 the kinematics of glaciotectonic thrusting. Fabrics of intact stratigraphy near the distal end of the
511 Rubjerg Knude thrust complex indicate that, before thrusting the LKF mud underwent
512 consolidation with longitudinal horizontal shortening. This shortening was moderate, as
513 indicated by clustering of k_1 and k_2 orientations perpendicular and parallel to the shortening
514 direction and by the lack of rotation of vertical k_3 orientations developed during mud deposition
515 and consolidation (Fig. 15).

516 AMS fabrics of thrust sheets of LKF mud within the Grønne Rende section of Rubjerg
517 Knude, indicate rotation of sheets mostly without internal deformation during thrusting. Within
518 decimeters of fault surfaces, however, mud was sheared to strains sufficient to overprint the LPS
519 fabric. The resultant fabric is observed consistently in ring-shear experiments conducted to large
520 displacements (> 0.5 m), with k_1 orientations parallel to shear and plunging mildly relative to the
521 shear plane. In thrust mud at Møns Klint, only rotation of LPS fabrics is observed, despite
522 samples collected as close as 3 cm to the chalk-mud contact. Slip, therefore, was seemingly
523 focused in a still narrower zone, with most of the thrust sheet behaving too rigidly to reset the
524 fabric.

525 Permafrost was not required for thrusting of intact sheets. If topographic surfaces of thrust
526 sheets sloped gently away from the glacier margin, a wide range of pore-water pressures could
527 have enabled slip on thrusts without internal deformation of individual thrust sheets. Shear
528 deformation observed close to faults at Rubjerg Knude may reflect elevated pore pressures in
529 mud adjacent to faults during thrusting.

530 **Acknowledgements**

531 We thank P.J. Hudleston and an anonymous reviewer for their helpful comments on the
532 manuscript, and Z. Kornse for his assistance with the field measurements. We also thank B.
533 Tikoff for the use of his Kappabridge at the University of Wisconsin-Madison and N. Garibaldi
534 for his help there.

535 536 **References**

- 537 Aber, J.S., 1980. Kineto-stratigraphy at Hvideklint, Møn, Denmark and its regional significance.
538 Bull. Geol. Soc. Denmark 28, 81-93.
- 539 Aber, J.S., 1982. Model for glaciotectionism. Bull. Geol. Soc. Denmark 30, 79-90.
- 540 Aber, J.S., Ber, A., 2007. Glaciotectionism, Elsevier, Amsterdam.
- 541 Almqvist, B.S.G., Koyi, H., 2018. Bulk strain in orogenic wedges based on insights from
542 magnetic fabrics in sandbox models. *Geology* 46(6), 483-486. [https://doi:
543 10.1130/G39998.1](https://doi.org/10.1130/G39998.1).
- 544 Ankerstjerne, S., Iverson, N.R., Lagroix, F., 2015. Origin of a washboard moraine of the Des
545 Moines Lobe inferred from sediment properties. *Geomorph.* 248, 452-463. [https://doi:
546 10.1016/j.geomorph.2015.07.019](https://doi.org/10.1016/j.geomorph.2015.07.019).
- 547 Averbuch, O., Lamotte, D.F. de, Kissel, C., 1992. Magnetic fabric as a structural indicator of the
548 Deformation path within a fold-thrust structure: a test case from the Corbières (NE

- 549 Pyrenees, France). *J. Struct. Geol.* 140(4), 461-474. <https://doi: 10.1016/0191->
550 8141(92)90106-7.
- 551 Bakhtari, H.R., Lamotte, D.F. de, Aubourg, C., Hassanzadeh, J., 1998. Magnetic fabrics of
552 Tertiary sandstones from the Arc of Fars (Eastern Zagros, Iran). *Tectonophys.* 284
553 (3-4), 299-316. [https://doi: 10.1016/S0040-1951\(97\)00179-0](https://doi: 10.1016/S0040-1951(97)00179-0).
- 554 Benediktsson, Í.Ö., Ingólfsson, Ó., Schomacker, A., Kjær, K.H., 2009. Formation of submarginal
555 and proglacial end moraines: implications of ice-flow mechanism during the 1963-64
556 surge of Brúarjökull, Iceland. *Boreas* 38(3), 440-457. <https://doi.org/10.1111/j.1502->
557 3885.2008.00077x.
- 558 Benediktsson, Í.Ö., Schomacker, A., Lokrantz, H., Ingólfsson, Ó., 2010. The 1890 surge end
559 moraine at Eyjabakkajökull, Iceland: a reassessment of a classic glaciotectionic locality.
560 *Quat. Sci. Rev.* 29(3-4), 484-506. <https://doi.org/10.1016/j.quascirev.2009.10.004>.
- 561 Benn, D.I., Clapperton, C.M., 2000. Pleistocene glaciotectionic landforms and sediments around
562 central Magellan Strait, southernmost Chile: evidence for fast outlet glaciers with cold-
563 based margins. *Quat. Sci.Rev.* 19(6), 591-612. <https://doi: 10.1016/S0277->
564 3791(99)00012-8.
- 565 Bennett, M.R., 2001. The morphology, structural evolution and significance of push moraines.
566 *Earth-Sci. Rev.* 53(3-4), 197-236. [https://doi.org/10.1016/S0012-8252\(00\)00039-8](https://doi.org/10.1016/S0012-8252(00)00039-8).
- 567 Borradaile, G.J., Henry, B., 1997. Tectonic applications of magnetic susceptibility and its
568 Anisotropy. *Earth-Sci. Rev.* 42(1-2), 49-93. [https://doi: 10.1016/S0012-8252\(96\)00044-](https://doi: 10.1016/S0012-8252(96)00044-)
569 X.
- 570 Boulton, G.S., Caban, P., 1995. Groundwater flow beneath ice sheets: Part II—its impact on

- 571 glacier tectonic structures and moraine formation. *Quat. Sci. Rev.* 14(6), 563-587.
572 [https://doi: 10.1016/0277-3791\(95\)00058-W](https://doi.org/10.1016/0277-3791(95)00058-W).
- 573 Boulton, G.S., van der Meer, D.J., Beets, D.J., Hart, J.K., Ruegg, G.H.J., 1999. The sedimentary
574 and structural evolution of a recent push moraine complex: Holmströmbreen,
575 Spitsbergen. *Quat. Sci. Rev.* 18(3), 339-371. [https://doi: 10.1016/S0277-3791\(98\)00068-](https://doi.org/10.1016/S0277-3791(98)00068-7)
576 7.
- 577 Burke, H., Phillips, E., Lee, J. R., Wilkinson, I. P., 2009. Imbricate thrust stack model for the
578 formation of glaciotectonic rafts: an example from the Middle Pleistocene of north
579 Norfolk, UK. *Boreas* 38, 620–637. <https://10.1111/j.1502-3885.2009.00085.x>. ISSN
580 0300-9483.
- 581 Caricchi, C., Cifelli, F., Kissel, C., Sagnotti, L., Mattei, M., 2016. Distinct magnetic fabric in
582 weakly deformed sediments from extensional basins and fold-and-thrust structures in the
583 Northern Apennine orogenic belt (Italy). *Tectonics*, 35(2), 238-256. [https:// doi:](https://doi.org/10.1002/2015TC003940)
584 10.1002/2015TC003940.
- 585 Clayton, L., Attig, J. W., Mickelson, D. M., 2001. Effects of late Pleistocene permafrost on the
586 landscape of Wisconsin, USA. *Boreas* 30, 173–188.
- 587 Collombat, C., Rochette, P., Vialon, P., 1995, Magnetic fabric as a strain indicator in
588 unconsolidated sediments of the Chile triple junction area. *Proc. Ocean Drilling Program,*
589 *Scientific Results* 141. College Station, Texas, Ocean Drilling Program, 9-49.
- 590 Croot, D.G., 1987. Glacio-tectonic structures: a mesoscale model of thin-skinned thrust sheets?
591 *J. Struct. Geol.* 9(7), 797-808. [https:// doi: 10.1016/0191-8141\(87\)90081-2](https://doi.org/10.1016/0191-8141(87)90081-2).
- 592 Davis, D., Suppe, J., Dahlen, F.A., 1983. Mechanics of fold and thrust belts and accretionary
593 wedges. *J. Geophys. Res.* 88(B2), 1153-1172.

- 594 Doblas, M., 1998. Slickenside kinematic indicators: *Tectonophys.* 295(1-2), 187-197.
595 [https://doi: 10.1016/S0040-1951\(98\)00120-6](https://doi:10.1016/S0040-1951(98)00120-6).
- 596 Feeser, V., 1988. On the mechanics of glaciotectionic contortion of clays, in: Croot, D.G. (Ed.),
597 *Glaciotectionics: Forms and Processes*. A.A. Balkema, Rotterdam, pp. 63-76.
- 598 Fleming, E.J., Lovell, H., Stevenson, C.T.E., Petronis, M.S., Benn, D.I., Hambrey, M.J.,
599 Fairchild, I.J., 2013a. Magnetic fabrics in the basal ice of a surge-type glacier. *J.*
600 *Geophys. Res. Earth Surf.* 118, 2263–2278, <https://doi:10.1002/jgrf.20144>.
- 601 Fleming, E.J., Stevensen, C.T.E., and Petronis, M.S., 2013b. New insights into the deformation
602 of a Middle Pleistocene glaciotectionised sequence in Norfolk, England, through magnetic
603 and structural analysis. *Proc. Geol. Assoc.* 124, 834-854.
- 604 Geocenter Møns Klint. <https://moensklint.dk/uk/nature/unesco-biosphere/>(accessed 6 January
605 2020).
- 606 Hicher, P.Y., Wahyudi, H., Tessier, D., 1994. Microstructural analysis of strain localization in
607 clay. *Computers and Geotechnics* 16(3), 205-222. [https:// doi: 10.1016/0266-](https://doi:10.1016/0266-352X(94)90002-7)
608 [352X\(94\)90002-7](https://doi:10.1016/0266-352X(94)90002-7).
- 609 Hooyer, T.S., Iverson, N.R., Lacroix, F., Thomason, J.F., 2008. Magnetic fabric of sheared till:
610 A strain indicator for evaluating the bed deformation model of glacier flow. *J. Geophys.*
611 *Res. Earth Surf.* 113. [https://doi: 10.1029/2007JF000757](https://doi:10.1029/2007JF000757).
- 612 Houmark-Nielsen, M., 1987. Pleistocene stratigraphy and glacial history of the central part of
613 Denmark. *Bull. Geol. Soc. Denmark* 36, 1-189.
- 614 Houmark-Nielsen, M., 1994. Late Pleistocene stratigraphy, glaciation chronology and Middle
615 Weichselian environmental history from Klintholm, Møn, Denmark. *Bull Geol. Soc.*
616 *Denmark* 41, 181-202.

- 617 Houmark-Nielsen, M., 1999. A lithostratigraphy of Weichselian glacial and interstadial deposits
618 in Denmark. *Bull. Geol. Soc. Denmark* 46, 101-114.
- 619 Houmark-Nielsen, M., 2007. Extent and age of Middle and Late Pleistocene glaciations and
620 periglacial episodes in southern Jylland, Denmark: *Bull. Geol. Soc. Denmark* 55, 9-35.
- 621 Houmark-Nielsen, M., 2008. Testing OSL failures against a regional Weichselian glaciation
622 chronology from southern Scandinavia. *Boreas* 37, 660-677.
- 623 Houmark-Nielsen, M., Kjær, K.H., 2003. Southwest Scandinavia, 40-15 kyr BP:
624 palaeogeography and environmental change. *J. Quat. Sci.* 18(8), 769-786. [https://doi:
625 10.1002/jqs.802.](https://doi.org/10.1002/jqs.802)
- 626 Housen, B.A., Kanamatsu, T., 2003. Magnetic fabrics from the Costa Rica margin: sediment
627 deformation during the initial dewatering and underplating process: *Earth Planet. Sci.*
628 *Lett.* 206(1-2), 215-228, [https://doi: 10.1016/S0012-821X\(02\)01076-2.](https://doi.org/10.1016/S0012-821X(02)01076-2)
- 629 Housen, B.A., Tobin, H.J., Labaume, P., Leitch, E.C., Maltman, A.J., 1996. Strain decoupling
630 across the decollement of the Barbados accretionary prism. *Geology*, 24(2), 127-130,
631 [https://doi.org/10.1130/0091-7613.](https://doi.org/10.1130/0091-7613)
- 632 Hudleston, P.J., 1992. Glacial movement and thrust emplacement, in: Mitra, S., Fisher, G.W.
633 (Eds), *Structural Geology of Fold and Thrust Belts*, Johns Hopkins University Press,
634 Baltimore, pp. 81-92.
- 635 Ingólfsson, Ó., 1988. Large-scale glaciotectonic deformation of soft sediments: a case study of a
636 late Weichselian sequence in western Iceland, in: Croot, D.G. (Ed), *Glaciotectonics:
637 Forms and Processes*, A.A. Balkema, Rotterdam, pp. 101-107.
- 638 Iverson, N.R., Baker, R.W., Hooyer, T.S., 1997. A ring-shear device for the study of till

- 639 deformation: tests on tills with contrasting clay contents. *Quat. Sci. Rev.* 16(9), 1057-
640 1066. [https://doi: 10.1016/S0277-3791\(97\)00036-X](https://doi.org/10.1016/S0277-3791(97)00036-X).
- 641 Iverson, N.R., Person, M., 2012. Glacier-bed geomorphic processes and hydrologic conditions
642 relevant to nuclear waste disposal. *Geofluids*, 12(1), 38-57. [https://doi: 10.1111/j.1468-](https://doi.org/10.1111/j.1468-8123.2011.00355.x)
643 8123.2011.00355.x.
- 644 Ives, L.R.W., and Iverson, N.R., 2019. Genesis of glacial flutes inferred from observations at
645 Múlajökull, Iceland. *Geology*, 47(5), 387-390, [https://doi.org /10 .1130 /G45714.1](https://doi.org/10.1130/G45714.1)
- 646 Jelínek, V., 1978. Statistical processing of anisotropy of magnetic susceptibility. *Studia*
647 *Geophysica et Geodaetica* 22(1), p. 50-62.
- 648 Jensen, J.B., 1993. Late Weichselian deglaciation pattern in the southwestern Baltic: Evidence
649 from glacial deposits off the island of Møn, Denmark. *Bull. Geol. Soc. Denmark* 40, 314-
650 331.
- 651 Jessen, A., 1899. Kortbladene Skagen, Hirtshals, Frederikshavn, Hjørring og Løkken. Danmarks
652 Geologiske Undersøgelse I. Række 3, 368 pp. + 5 maps.
- 653 Johnstrup, F., 1874. Über die Lagerungsverhältnisse und die Hebungs-phänomene in den
654 Kreidefeldern auf Mön und Rügen. *Zeitschrift der deutschen geologischen Gesellschaft*
655 1874, 533-585.
- 656 Johnstrup, F., 1882. Om de geologiske forhold i den nordlige del af Vendsyssel.
657 Universitetsprogram, Kjøbenhavn.
- 658 Klint, K.E.S., Nilsson, B., Troldborg, L., Jakobsen, P.R., 2013. A polymorphological landform
659 approach for hydrogeological applications in heterogeneous glacial sediments. *Hydro. J.*,
660 21(6), 1247-1264. [https://doi: 10.1007/s10040-013-1011-2](https://doi.org/10.1007/s10040-013-1011-2).
- 661 Kołodziejczyk, U., Kostecki, J., Gontaszewska-Piekarz, A., Wysokowski, A., 2018. The problem

- 662 of stabilization of landslides in glaciotectonically disturbed areas. Case study: road
663 engineering structure, in VI International Conference of Science and Technology
664 INFRAEKO 2018 Modern Cities. Infrastructures and Environment. Krakow, Poland,
665 Volume 45, 8 pp., <https://doi:10.1051/e3sconf/20184500032>.
- 666 Kuriger, E.M., Truffer, M., Motyka, R.J., Bucki, A.K., 2006. Episodic reactivation of large-scale
667 push moraines in front of the advancing Taku Glacier, Alaska. *J. Geophys. Res.* 111,
668 [https://doi: 10.1029/2005JF000385](https://doi:10.1029/2005JF000385).
- 669 Lowe, D.R., 1975. Water escape structures in coarse-grained sediments. *Sediment.* 22(2),
670 157-204. [https://doi: 10.1111/j.1365-3091.1975.tb00290.x](https://doi:10.1111/j.1365-3091.1975.tb00290.x).
- 671 Mathews, W.H., Mackay, J.R., 1960. Deformation of soils by glacier ice and the influence of
672 pore pressures and permafrost. *Trans. Roy. Soc. Can.* 54, 27–36.
- 673 Mark, D.M., 1973. Analysis of axial orientation data, including till fabrics: *Bull. Geol. Soc.*
674 *Am.* 84(4),1369-1374. [https:// doi: 10.1130/0016-](https://doi:10.1130/0016-7606(1973)84<1369:AOAODI>2.0.CO;2)
675 [7606\(1973\)84<1369:AOAODI>2.0.CO;2](https://doi:10.1130/0016-7606(1973)84<1369:AOAODI>2.0.CO;2).
- 676 McCracken, R.G., Iverson, N.R., Benediktsson, Í.Ö., Schomacker, A., Zoet, L.K., Johnson,
677 M.D., Hooyer, T.S., Ingólfsson, Ó., 2016. Origin of the active drumlin field at
678 Múlajökull, Iceland: New insights from till shear and consolidation patterns. *Quat. Sci.*
679 *Rev.* 148, 243-260. [https://doi: 10.1016/j.quascirev.2016.07.008](https://doi:10.1016/j.quascirev.2016.07.008).
- 680 Menzies, J., 1990. Sand intraclasts within a diamicton mélange, southern Niagara Peninsula,
681 Ontario, Canada. *J. Quat. Sci.* 5, 189-206.
- 682 Mooers, H.D., 1990. Ice-marginal thrusting of drift and bedrock: thermal regime, subglacial
683 aquifers, and glacial surges. *Can. J. Earth Sci.* 27(6), 849-862. [https://doi: 10.1139/e90-](https://doi:10.1139/e90-088)
684 [088](https://doi:10.1139/e90-088).

- 685 Moore, P. L., 2014. Deformation of debris-ice mixtures. *Rev. Geophys.* 52, 435–467.
686 <https://doi:10.1002/2014RG000453>.
- 687 Moran, S.R., Clayton, L., Hooke, R.L., Fenton, M.M., Andriashek, L.D., 1980. Glacier-bed
688 landforms of the prairie region of North American. *J. Glaciol.* 25, 457-476. [https://doi:](https://doi:10.3189/S0022143000015306)
689 [10.3189/S0022143000015306](https://doi:10.3189/S0022143000015306).
- 690 Morgenstern, N.R., Tchalenko, J.S., 1967. Microscopic structures in kaolin subjected to direct
691 Shear. *Géotechnique* 17(4), 309-328. [https://doi: 10.1680/geot.1967.17.4.309](https://doi:10.1680/geot.1967.17.4.309).
- 692 Parés, J.P., 2015. Sixty years of anisotropy of magnetic susceptibility in deformed sedimentary
693 rocks. *Front. Earth Sci.* 3, <https://doi.org/10.3389/feart.2015.00004>.
- 694 Pedersen, S.A.S., 2000. Superimposed deformation in glaciotectonics. *Bull. Geol.*
695 *Soc. Denmark* 46, 125-144.
- 696 Pedersen, S.A.S., 2005. Structural analysis of the Rubjerg Knude glaciotectonic complex,
697 Vendsyssel, northern Denmark. *Geological Survey of Denmark and Greenland* 8, 192 pp.
- 698 Pedersen, S.A.S., 2014. Architecture of Glaciotectonic Complexes. *Geosciences* 4, 269-296.
699 [doi:10.3390/geosciences4040269](https://doi.org/10.3390/geosciences4040269)
- 700 Pedersen, S.A.S., Gravesen, P., 2009. Structural development of Maglevandsfald: a key to
701 understanding the glaciotectonic architecture of Møns Klint, SE Denmark. *Geological*
702 *Survey of Denmark and Greenland*, v. 17, p. 29-32.
- 703 Pedersen, S.A.S., Møller, I., 2004. Prediction and risk evaluation of chalk cliff collapse: the
704 PROTECT project. *Bull. Geol. Soc. Denmark* 4, 89-92.
- 705 Petit, J.P., 1987. Criteria for the sense of movement on fault surfaces in brittle rocks. *J.*
706 *Struct. Geol.* 9(5-6), 597-608. [https://doi: 10.1016/0191-8141\(87\)90145-3](https://doi:10.1016/0191-8141(87)90145-3).

Revised April 23, 2020

- 707 Phillips, E.R., 2018. Glacitectonics, in Menzies, J. and van der Meer, J., (Ed., Past Glacial
708 Environments, 2nd edition. Elsevier, Amsterdam. [https://doi.org/10.1016/B978-0-08-
709 100524-8.00014-2](https://doi.org/10.1016/B978-0-08-100524-8.00014-2).
- 710 Puggaard, C., 1851. Møens Geologie. Universitetets Guldmedaille Priisskrift. København.
711 Reitzel, 287 pp.
- 712 Sadolin, M., Pedersen, G.K., Pedersen, S.A.S., 1997. Lacustrine sedimentation and tectonics: an
713 example from the Weichselian at Lønstrup Klint, Denmark. *Boreas*, 26(2), 113-126.
714 [https://doi: 10.1111/j.1502-3885.1997.tb00658.x](https://doi:10.1111/j.1502-3885.1997.tb00658.x).
- 715 Saint-Bezar, B., Hebert, R.L., Aubourg, C., Robion, P., Swennen, R., de Lamotte, D.F., 2002.
716 Magnetic fabric and petrographic investigation of hematite-bearing sandstones within
717 ramp-related folds: examples from the South Atlas Front (Morocco). *J. of Struct. Geol.*,
718 24(9), 1507-1520. [https://doi: 10.1016/S0191-8141\(01\)00140-7](https://doi:10.1016/S0191-8141(01)00140-7).
- 719 Seidenkrantz, M-S., Knudsen, K.L., 1993. Middle Weichselian to Holocene palaeocology in the
720 eastern Kattegat, Scandinavia: foraminifera, ostracods and 14C measurements. *Boreas*
721 22(4), 299-310. [https://doi: 10.1111/j.1502-3885.1993.tb00190.x](https://doi:10.1111/j.1502-3885.1993.tb00190.x).
- 722 Shumway, J.R., Iverson, N.R., 2009. Magnetic fabrics of the Douglas Till of the Superior lobe:
723 exploring bed-deformation kinematics. *Quat. Sci. Rev.* 28(1-2), 107-119. [https://doi:
724 10.1016/j.quascirev.2008.09.020](https://doi:10.1016/j.quascirev.2008.09.020).
- 725 Sjørring, S., 1977. The glacial stratigraphy of the island of Als, southern Denmark. *Zeits.*
726 *Geomorph.* 27, 1-11.
- 727 Sollid, J.L., Sørbel, L., 1988. Influence of temperature conditions in formation of end moraines
728 in Fennoscandia and Svalbard. *Boreas* 17, 553–558.
- 729 Talbot, C.J., 199. Ice ages and nuclear waste isolation. *Eng. Geol.* 52, 177–99.

- 730 Tarling, D., Hrouda, F., 1993. *The Magnetic Anisotropy of Rocks*. Springer
731 Science & Business Media, London.
- 732 Thomas, G.S.P., 1984. The origin of the glacio-dynamic structure of the Bride Moraine, Isle of
733 Man. *Boreas* 13, 355–364.
- 734 Thomason, J.F., Iverson, N.R., 2009. Deformation of the Batestown Till of the Lake Michigan
735 Lobe. *J. Glaciol.* 55, 131-146.
- 736 Turcotte, D., Schubert, G., 2002. *Geodynamics*. Cambridge University Press, Cambridge.
- 737 Van der Wateren, F.M., 2002. Processes of glaciotectonism, in: Menzies, J. (Ed.), *Modern and*
738 *Past Glacial Environments*. Butterworth-Heinemann, Oxford, pp. 417-443.
- 739 Vreeland, N.P., Iverson, N.R., Graesch, M., Hooyer, T.S., 2015. Magnetic fabrics of drumlins of
740 the Green Bay Lobe, southeastern Wisconsin. *Quat. Sci. Rev.* 112, 33-44.
- 741 Wang, J., Nishimura, S., 2018. Interpretation of mechanical behavior of frozen clay through
742 parallel tests of frozen and unfrozen soils. *Jap. Geotech. Soc. Spec. Publ.* 5(2), 155-160.
743 [https://doi: 10.3208/jgssp.v05.042](https://doi.org/10.3208/jgssp.v05.042).
- 744 Warbritton, M., 2019. Strain patterns in the Møns Klint and Rubjerg Knude glaciotectonic
745 complexes, Denmark, inferred from anisotropy of magnetic susceptibility. M.S. thesis,
746 Iowa State University.

747

748 **Appendix: Magnetic mineralogy**

749

750 Interpreting anisotropy of magnetic susceptibility (AMS) data requires a priori knowledge of
751 the mineral composition of the analyzed samples. Specifically, assessing whether paramagnetic
752 minerals, ferrimagnetic minerals or a combination of both control the AMS is crucial. The AMS
753 of paramagnetic minerals is dictated by the mineral's crystal symmetry and is said to have a

754 crystallographic preferred orientation. Ferrimagnetic mineral particles with high saturation
755 magnetizations, such as magnetite and maghemite, have AMS controlled by the shape of the
756 particle and are said to have a preferred shape orientation (Tarling and Hrouda, 1993). Rock
757 magnetic analyses at room temperature and low-temperature were conducted at the *Institut de*
758 *Physique du Globe de Paris* (France) in order to determine whether magnetite (or maghemite)
759 were present and at what concentration.

760 Representative bulk samples from Rubjerg Knude (RK3) and Møns Klint (MUN01) were
761 analyzed. Each bulk sample was homogenized using an agate mortar and pestle and dried at
762 40°C overnight. The powdered bulk samples were then firmly packed in 0.21 ml gelatin capsules
763 (14.3 mm in length and 5 mm in diameter). The RK3 and MUN01 subsamples contained 434.4
764 mg and 476.6 mg, respectively, of bulk material.

765 Two room-temperature experiments were conducted on a Princeton Measurements Model
766 3900 Vibrating Sample Magnetometer (VSM). First, hysteresis loops and initial magnetizations
767 curves were measured in maximum magnetic fields of ± 1.5 T. Mass-specific low-field magnetic
768 susceptibility was calculated from the initial slope of the first magnetization curves. Saturation
769 magnetization, saturation remanent magnetization, coercivity and high field magnetic
770 susceptibility were derived from the hysteresis loops after correction for the high field slopes.
771 Second, an isothermal remanent magnetization (IRM) acquisition curve was measured on
772 demagnetized subsamples by acquiring IRMs in progressively increasing magnetic fields from
773 zero to 1.5 T with 200 logarithmically spaced steps.

774 Two low-temperature experiments were conducted on a Magnetic Properties Measurement
775 System (MPMS) XL-5 Evercool. First a room-temperature (300 K) IRM was acquired in a 2.5 T
776 magnetic field and measured as the subsample was cooled to 10 K and warmed back to 300 K at

777 a rate of 5 K/min. The second experiment measures a low-temperature (10 K) IRM acquired in a
778 2.5 T magnetic field as the subsample is warmed from 10 K to 300 K at a rate of 5 K/min. The
779 10 K IRM is acquired following one of two pre-treatments. The zero-field cooled (ZFC) pre-
780 treatment cools the subsample from 300 K to 10 K in zero (< 500 nT) magnetic field before
781 acquiring the 10 K IRM and the field cooled (FC) pre-treatment cools the subsample from 300 K
782 to 10 K in a 2.5 T magnetic field before acquiring the 10 K IRM.

783 The hysteresis loop and first magnetization derived parameters are listed in Table A1 and
784 hysteresis loops before and after correction shown in Figure A1. Low-field magnetic
785 susceptibility, inclusive of all minerals, of RK3 and MUN01 are quite similar 20×10^{-8} and $17 \times$
786 10^{-8} m³/kg. However, the high-field magnetic susceptibility of RK3, which excludes
787 ferromagnetic (sensus lato) that have saturated (primarily ferrimagnetic minerals), is more than 3
788 times the value for MUN01. Saturation magnetization values confirm the higher concentration of
789 ferrimagnetic minerals in MUN01 with values twice those of RK3. Squareness and coercivity
790 ratios of RK3 and MUN01 are in agreement with a population of ferrimagnetic magnetic domain
791 sizes larger than single domain. Therefore, inverse AMS fabrics are not expected.

792 The low temperature experiments shown in Figure A2 confirm that magnetite is the dominant
793 ferrimagnetic mineral present in both RK3 and MUN01 subsamples. The Verwey transition,
794 which is characteristic of stoichiometric magnetite, is observed by a sharp drop in remanence at
795 120 K in the ZFC and FC 10 K IRM warming curves. The 300 K IRM cooling and warming
796 cycles display more broadly but just as convincingly the Verwey transition. The remanence loss
797 and gain in Figure A2A is identical in both samples, which attests to the very similar magnetic
798 domain states of the magnetite population contributing to the AMS at Rubjerg Knude and Møns
799 Klint.

800 Since magnetite is shown to be the dominant ferrimagnetic mineral, saturation magnetization
801 values, which are independent of magnetic domain size (i.e. particle size) unlike remanent
802 magnetization, can be used to calculate weight percent concentration of magnetite. The intrinsic
803 saturation magnetization of stoichiometric magnetite is $92 \text{ Am}^2/\text{kg}$ at room temperature (Dunlop
804 and Özdemir, 1997). Assuming that stoichiometric magnetite is the sole contributor to the
805 saturation magnetization RK3 contains 0.01 wt. % magnetite and MUN01, 0.03 wt. % magnetite.

806 In conclusion, magnetite is the dominant ferrimagnetic mineral in both RK3 and MUN01. The
807 magnetite population grain-size distributions are similar at both sites and fall well into the
808 pseudo single-domain to small multi-domain particle size range. Inverse AMS fabrics are
809 therefore not expected. Magnetite concentrations are low, 0.01 wt% at Rubjerg Knude and 0.03
810 wt% at Møns Klint but similar, for example, to the 0.03 wt.% magnetite calculated for the
811 Batestown Till (Hooyer et al. 2008) in which magnetite controlled AMS fabrics.

812
813 **Figure captions**

814
815 **Figure 1.** Locations of the two glacitectonic complexes. Black line indicates the “Main
816 Stationary Line,” i.e., the extent of the Scandinavian Ice Sheet during the last glacial
817 maximum (~20 ka before present). The red line shows the maximum extent of the Norwegian
818 Ice Advance at 28 ka before present (modified from Pedersen, 2005).

819 **Figure 2.** (A) Schematic cross-sections of the Rubjerg Knude complex, The three thrust sheets
820 studied, as numbered by Pedersen (2005), are indicated. The complex’s (B) Grønne Rende
821 section, and its (C) distal Ulstrup section, with ~1.2 vertical exaggeration. RKF and LKF refer
822 to Rubjerg Knude and Lønstrup Klint Formations, respectively (see text) (modified from
823 Pedersen (2005).

824 **Figure 3.** Thrusted mud sheets of the Lønstrup Klint Formation (grey) with intervening sand and
825 gravel of the Rubjerg Knude Formation (brown), within the Grønne Rende section at Rubjerg
826 Knude. The thrusted mud sheet at center-right is GR07 (see Fig. 2B). Note person for scale
827 in the right-hand side of the photograph.

828 **Figure 4.** (A) Oblique photograph of the east coast of the island of Møn, Denmark (from
829 GeoCenter Møns Klint), showing the chalk of Møns Klint and the location of the thrust fault
830 studied. (B) Chalk (white) thrust over the glaciolacustrine mud (grey) sampled at Møns Klint.
831 Dashed line indicates the contact, with colluvium at lower right.

832 **Figure 5.** Aluminum sample boxes pushed into the glaciolacustrine mud at Møns Klint,
833 immediately underlying the Upper Cretaceous chalk that has been thrust over it from left to
834 right. After excavation of the boxes, the mud was transferred to plastic boxes for storage,
835 sealing, and subsequent AMS analysis.

836 **Figure 6.** View normal to the surface of a thrust fault at the base of sheet GR10 in the Grønne
837 Rende section at Rubjerg Knude, showing slickensides at the base of the mud layer. The mud
838 was thrust upward in the photograph, over sand that has been cleared to expose the fault
839 surface. The treads on the stepped fault surface are P fractures. Mallet head for scale.

840 **Figure 7.** (A) Mud and sand of the Lønstrup Klint Formation thrust along a slickensided fault
841 surface (dashed red line) and over sand of the Rubjerg Knude Formation, within the Grønne
842 Rende section at Rubjerg Knude, thrust sheet GR10 (Fig. 2). The area of overthrust
843 sediment outlined in yellow was sampled for AMS, at various distances from the fault
844 surface. (B) The mud sheet of GR05 thrust along slickensided fault surfaces (red). AMS
845 samples were collected at various distances from the fault over transects A, B and C.

846 **Figure 8.** Upper Cretaceous chalk overlying glaciolacustrine mud of the Middle Weichselian at
847 Møns Klint, with intervening fault indicated by the red dashed line. AMS samples were
848 gathered along transects A-D. Dark grey areas are where fresh mud has been exposed for
849 sampling; light grey areas are the weathered and un-sampled mud surface. Colluvium is in the
850 foreground.

851 **Figure 9.** (A) Orientations of the three principal magnetic susceptibilities of the mud from
852 Rubjerg Knude after it had been sheared in a ring-shear device to a displacement of 0.6 m.
853 Arrows at upper left indicate sense of shear. (B) Orientations of principal susceptibilities from
854 a similar experiment conducted to a displacement of 0.5 m on a till deposited subglacially and
855 derived from remobilized glaciolacustrine mud (Douglas till, Hooyer et al., 2008; Shumway
856 and Iverson, 2009). Large orange symbols show V_1 eigenvectors calculated from the
857 principal-susceptibility distributions.

858 **Figure 10.** Principal-susceptibility orientations for the six fabrics from the distal end of the
859 Rubjerg Knude thrust complex (Ulstrup section). Large orange symbols show V_1 eigenvectors
860 calculated from the principal-susceptibility distributions.

861 **Figure 11.** Aggregated principal susceptibility orientations at Rubjerg Knude. (A) Principal-
862 susceptibility orientations aggregated for fabrics from the distal end of the thrust complex
863 (Ulstrup section). S_1 values for k_1 , k_2 and k_3 are 0.86, 0.81 and 0.89, respectively. (B)
864 Principal-susceptibility orientations aggregated for fabrics within ~0.1 m and ~0.7 m of the
865 GR10 and GR05 fault surfaces, respectively, within the Grønne Rende section. S_1 values for
866 k_1 , k_2 and k_3 are 0.78, 0.77 and 0.92, respectively. (C) Principal-susceptibility orientations
867 aggregated for fabrics more than 0.1 m and ~0.7 m away from the GR10 and GR05 fault
868 surfaces, respectively. S_1 values for k_1 , k_2 and k_3 are 0.81, 0.80 and 0.92, respectively. (D)

869 Principal-susceptibility orientations aggregated for fabrics from eroded dip-slope surfaces
870 away from faults. S_1 values for k_1 , k_2 and k_3 are 0.0.76, 0.73 and 0.85, respectively. Large
871 orange symbols show V_1 eigenvectors calculated from the principal-susceptibility
872 distributions.

873 **Figure 12.** Four fabrics from thrust sheet GR10 from the Grønne Rende section of Rubjerg
874 Knude. Distances listed are relative to the adjacent fault surface. The fault orientation is
875 shown in a lower-hemisphere stereonet at upper-right, and the cyan arrow shows the ice-
876 advance direction. Large orange symbols show V_1 eigenvectors calculated from the principal-
877 susceptibility distributions.

878 **Figure 13.** Nine fabrics from transects A, B, and C in the thrust sheet GR05 from the Grønne
879 Rende section of Rubjerg Knude (see Fig. 7B for transects). Distances listed are relative to the
880 nearest fault surface. The fault orientation is shown in a lower-hemisphere stereonet at upper-
881 right, and the cyan arrow shows the ice-advance direction. Large orange symbols show V_1
882 eigenvectors calculated from the principal-susceptibility distributions.

883 **Figure 14.** Principal-susceptibility orientations for 17 AMS fabrics collected in the four
884 transects at Møns Klint (see Figure 8), aggregated for five distance ranges from the fault at the
885 chalk-mud boundary. The fault orientation is shown in a lower-hemisphere stereonet at upper-
886 right, and the cyan arrow shows the ice-advance direction. Large orange symbols show V_1
887 eigenvectors calculated from the principal-susceptibility distributions.

888 **Figure 15.** Model for AMS fabric development during deposition/consolidation and layer-
889 parallel shortening (modified from Almqvist and Koyi, 2018).

890 **Figure 16.** Schematic diagram of a thrust wedge subject to a push, σ_x (modified from Davis et
891 al., 1983).

892 **Figure 17.** Threshold values of pore-pressure ratio, λ , and topographic slope of the thrust wedge,
893 α , above which slip is expected on thrusts without internal deformation of thrust sheets, for
894 different values of thrust dip, β . Zero internal cohesion, $\lambda_b = \lambda$, and $\mu_b = \mu = \tan \varphi$ are
895 assumed, making estimates of λ and α required for slip without internal deformation
896 conservatively large. Also assumed are $\sin \alpha \approx \alpha$ and $\sin \beta \approx \beta$, good to within 5% for the
897 largest angles considered ($\beta = 30^\circ$). The hydrostatic value of $\lambda = p_w / \sigma_z$ is based on a
898 groundwater table at the ground surface, a sediment porosity of 50%, and rock particle density
899 of 2700 kg m^{-3} .

900 **Figure A1.** (A) Hysteresis loops for samples from Rubjerg Knude (RK3) and Møns Klint
901 (MUN01) before and after correction. (B) Detail of loops within inset shown in (A).

902 **Figure A2.** Results of low temperature experiments for samples from Rubjerg Knude (RK3) and
903 Møns Klint (MUN01). (A) 300 K IRM cooling and warming cycles. (B) IRM warming
904 curves.

905
906
907
908
909
910
911
912
913
914
915
916
917
918
919
920
921
922
923
924

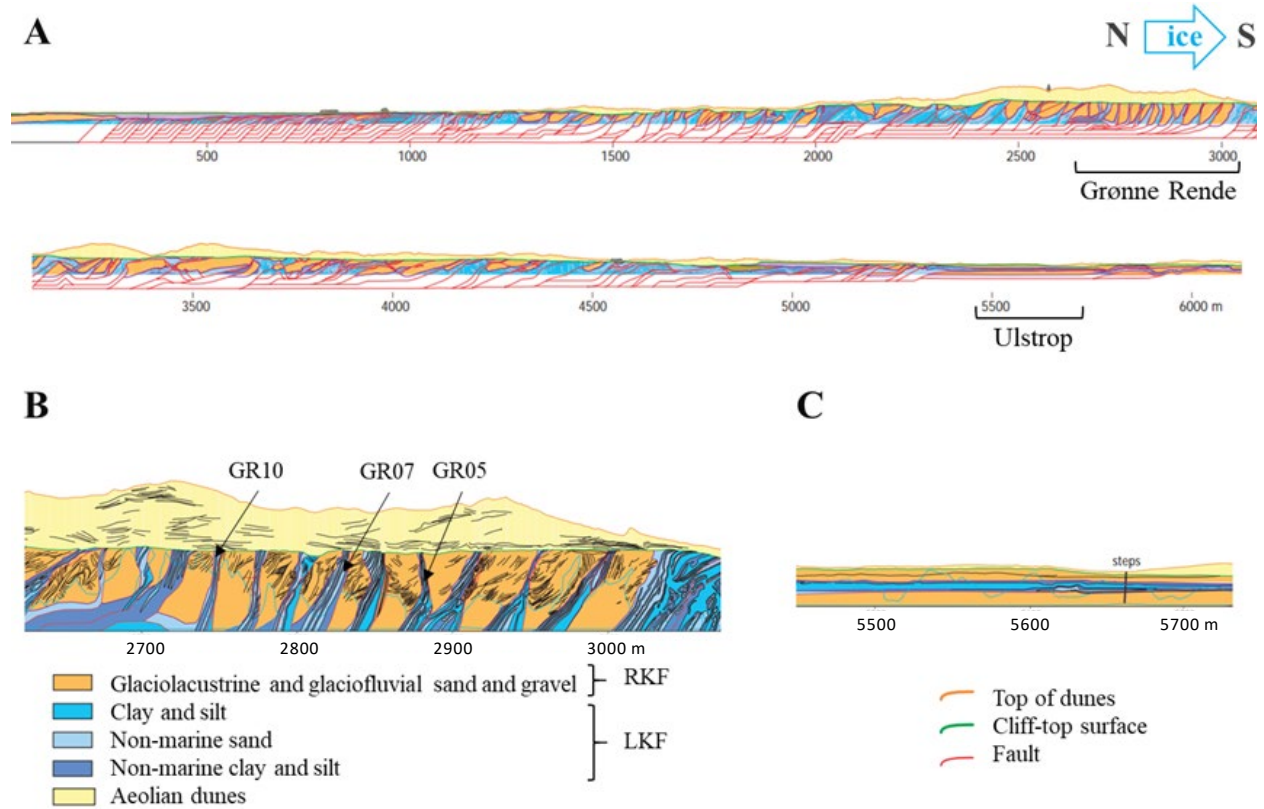
925 **Figures**
926



927
928
929

930 **Figure 1.** Locations of the two glacial complexes. Black line indicates the “Main
931 Stationary Line,” i.e., the extent of the Scandinavian Ice Sheet during the last glacial
932 maximum (~20 ka before present). The red line shows the maximum extent of the Norwegian
933 Ice Advance at 28 ka before present (modified from Pedersen, 2005).

934
935
936
937
938
939
940



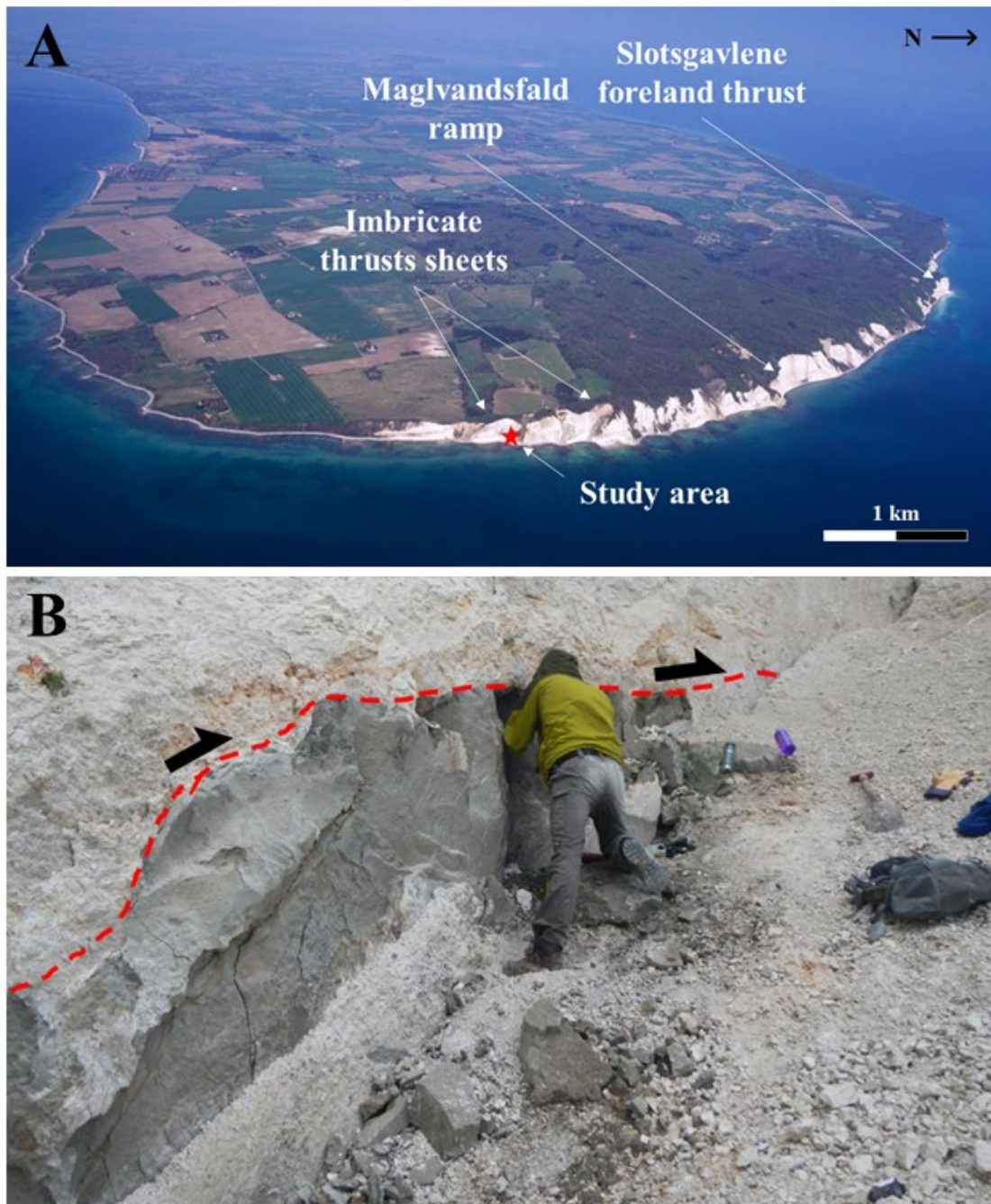
941
942
943
944
945
946
947
948
949
950
951
952
953
954
955
956
957
958
959

Figure 2. (A) Schematic cross-sections of the Rubjerg Knude complex, The three thrust sheets studied, as numbered by Pedersen (2005), are indicated. The complex's (B) Grønne Rende section, and its (C) distal Ulstrup section, with ~1.2 vertical exaggeration. RKF and LKF refer to Rubjerg Knude and Lønstrup Klint Formations, respectively (see text) (modified from Pedersen (2005)).



960
961
962
963
964
965
966
967
968
969
970
971
972
973
974
975
976
977
978
979

Figure 3. Thrusted mud sheets of the Lønstrup Klint Formation (grey) with intervening sand and gravel of the Rubjerg Knude Formation (brown), within the Grønne Rende section at Rubjerg Knude. The thrusted mud sheet at center-right is GR07 (see Fig. 2B). Note person for scale in the right-hand side of the photograph.



980
981
982
983
984
985
986
987
988
989

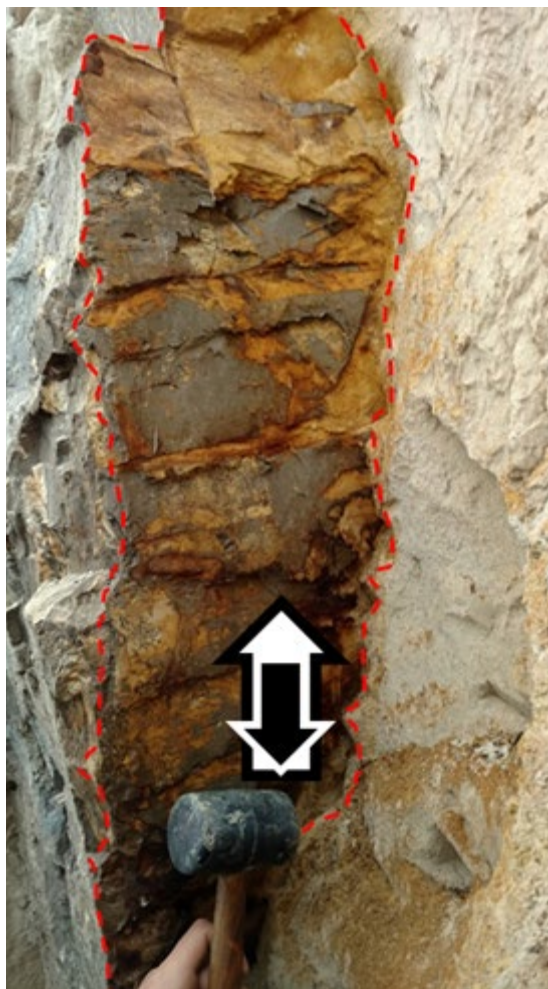
Figure 4. (A) Oblique photograph of the east coast of the island of Møn, Denmark (from GeoCenter Møns Klint), showing the chalk of Møns Klint and the location of the thrust fault studied. (B) Chalk (white) thrust over the glaciolacustrine mud (grey) sampled at Møns Klint. Dashed line indicates the contact, with colluvium at lower right.

990
991
992
993
994
995



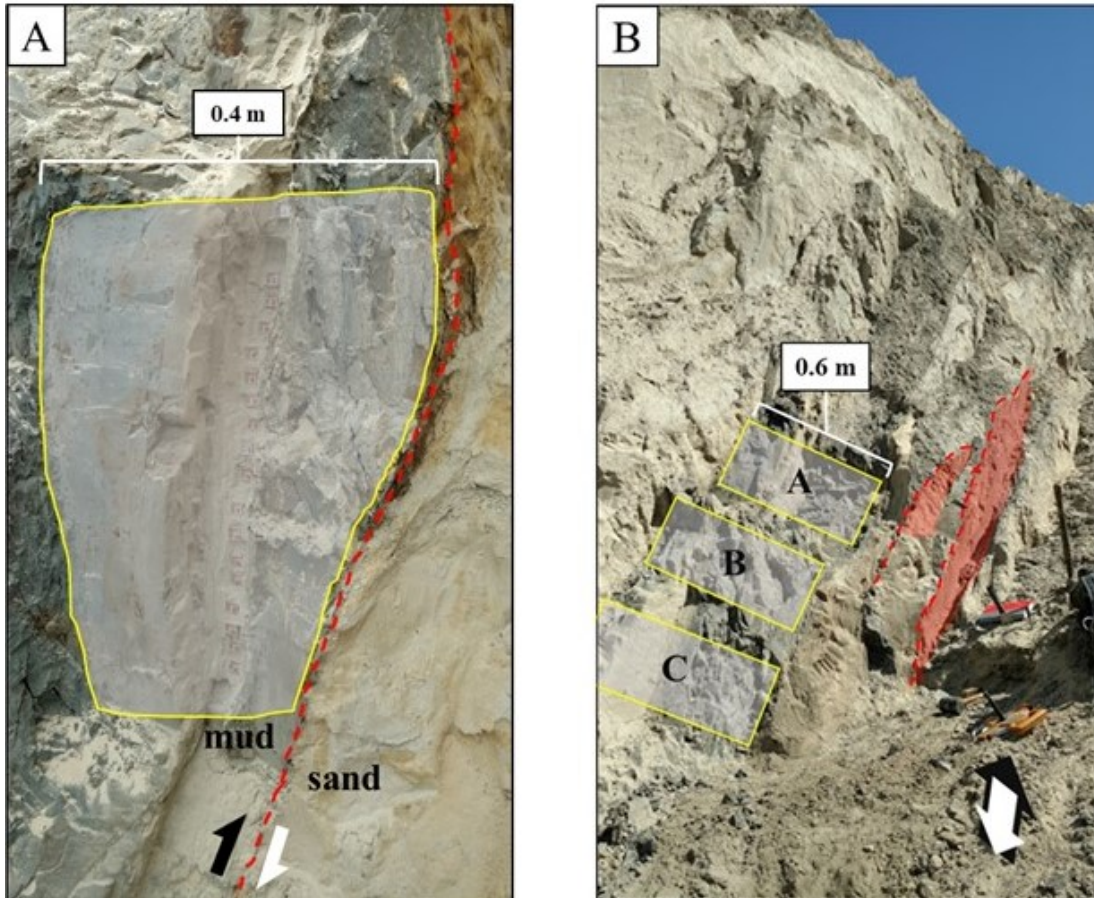
996
997
998
999
1000
1001
1002
1003
1004
1005
1006
1007
1008
1009
1010
1011
1012
1013
1014

Figure 5. Aluminum sample boxes pushed into the glaciolacustrine mud at Møns Klint, immediately underlying the Upper Cretaceous chalk that has been thrust over it from left to right. After excavation of the boxes, the mud was transferred to plastic boxes for storage, sealing, and subsequent AMS analysis.



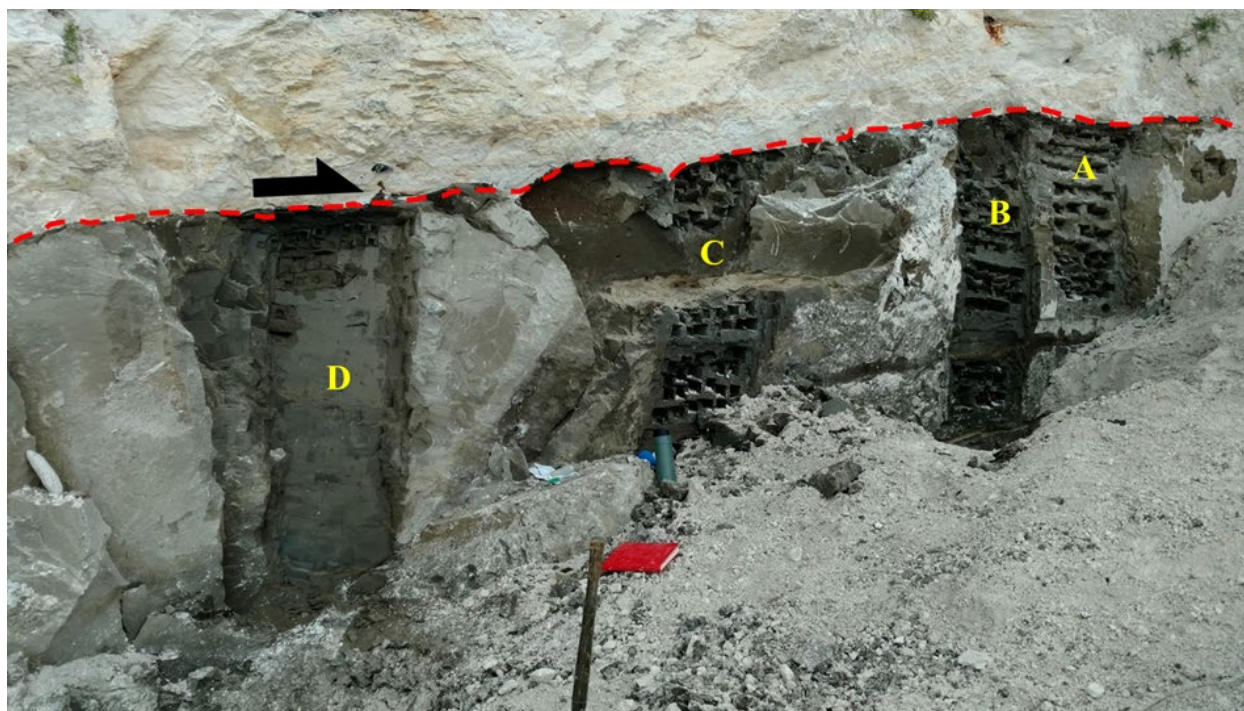
1015
1016
1017
1018
1019
1020
1021
1022
1023
1024
1025
1026
1027
1028

Figure 6. View normal to the surface of a thrust fault at the base of sheet GR10 in the Grønne Rende section at Rubjerg Knude, showing slickensides at the base of the mud layer. The mud was thrust upward in the photograph, over sand that has been cleared to expose the fault surface. The treads on the stepped fault surface are P fractures. Mallet head for scale.



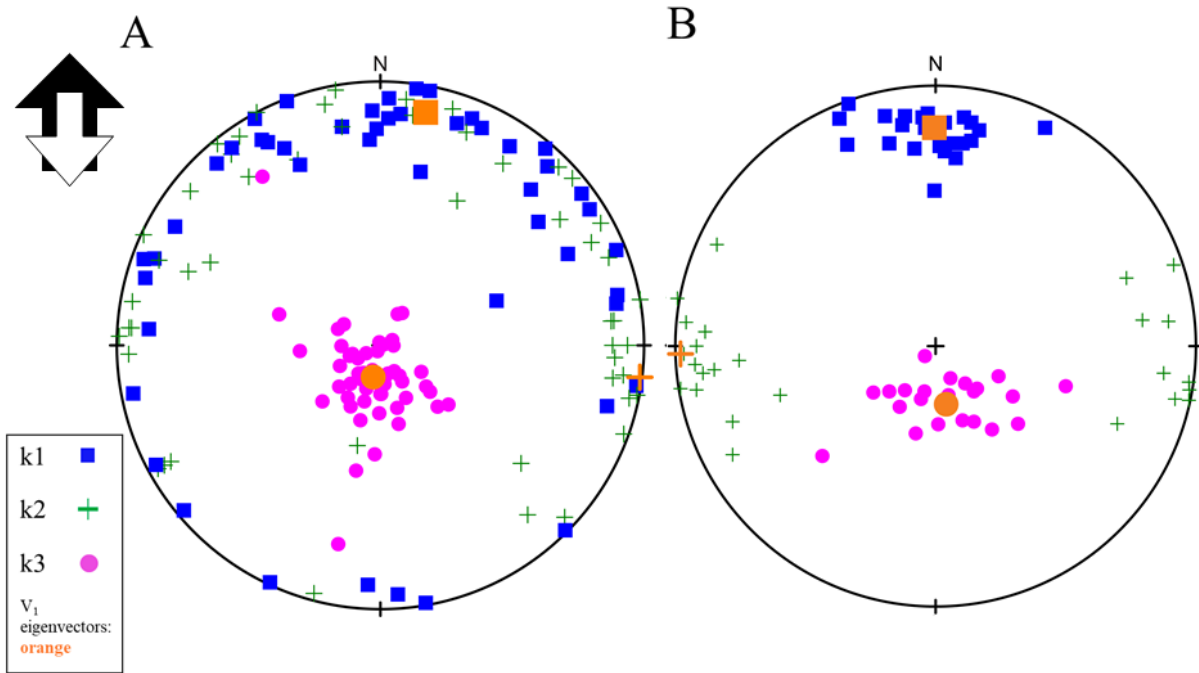
1029
1030
1031
1032
1033
1034
1035
1036
1037
1038
1039
1040
1041
1042
1043
1044

Figure 7. (A) Mud and sand of the Lønstrup Klint Formation thrust along a slickensided fault surface (dashed red line) and over sand of the Rubjerg Knude Formation, within the Grønne Rende section at Rubjerg Knude, thrust sheet GR10 (Fig. 2). The area of overthrust sediment outlined in yellow was sampled for AMS, at various distances from the fault surface. (B) The mud sheet of GR05 thrust along slickensided fault surfaces (red). AMS samples were collected at various distances from the fault over transects A, B and C.



1045
1046
1047
1048
1049
1050
1051
1052
1053
1054
1055
1056
1057
1058
1059
1060
1061

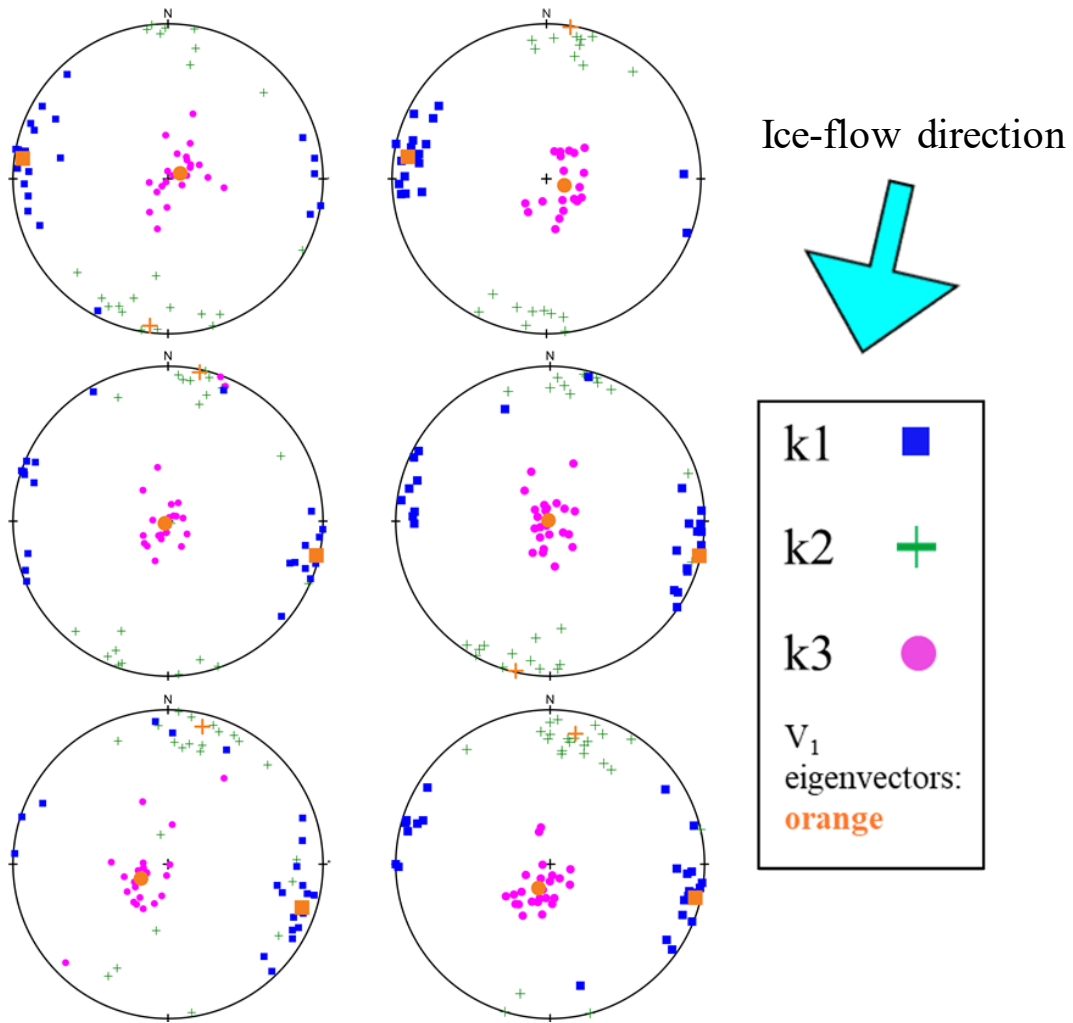
Figure 8. Upper Cretaceous chalk overlying glaciolacustrine mud of the Middle Weichselian at Møns Klint, with intervening fault indicated by the red dashed line. AMS samples were gathered along transects A-D. Dark grey areas are where fresh mud has been exposed for sampling; light grey areas are the weathered and un-sampled mud surface. Colluvium is in the foreground.



1062
 1063
 1064
 1065
 1066
 1067
 1068
 1069
 1070
 1071
 1072
 1073
 1074
 1075
 1076
 1077
 1078
 1079
 1080
 1081
 1082
 1083

Figure 9. (A) Orientations of the three principal magnetic susceptibilities of the mud from Rubjerg Knude after it had been sheared in a ring-shear device to a displacement of 0.6 m. Arrows at upper left indicate sense of shear. (B) Orientations of principal susceptibilities from a similar experiment conducted to a displacement of 0.5 m on a till deposited subglacially and derived from remobilized glaciolacustrine mud (Douglas till, Hooyer et al., 2008; Shumway and Iverson, 2009). Large orange symbols show V_1 eigenvectors calculated from the principal-susceptibility distributions.

1084



1085

1086

1087

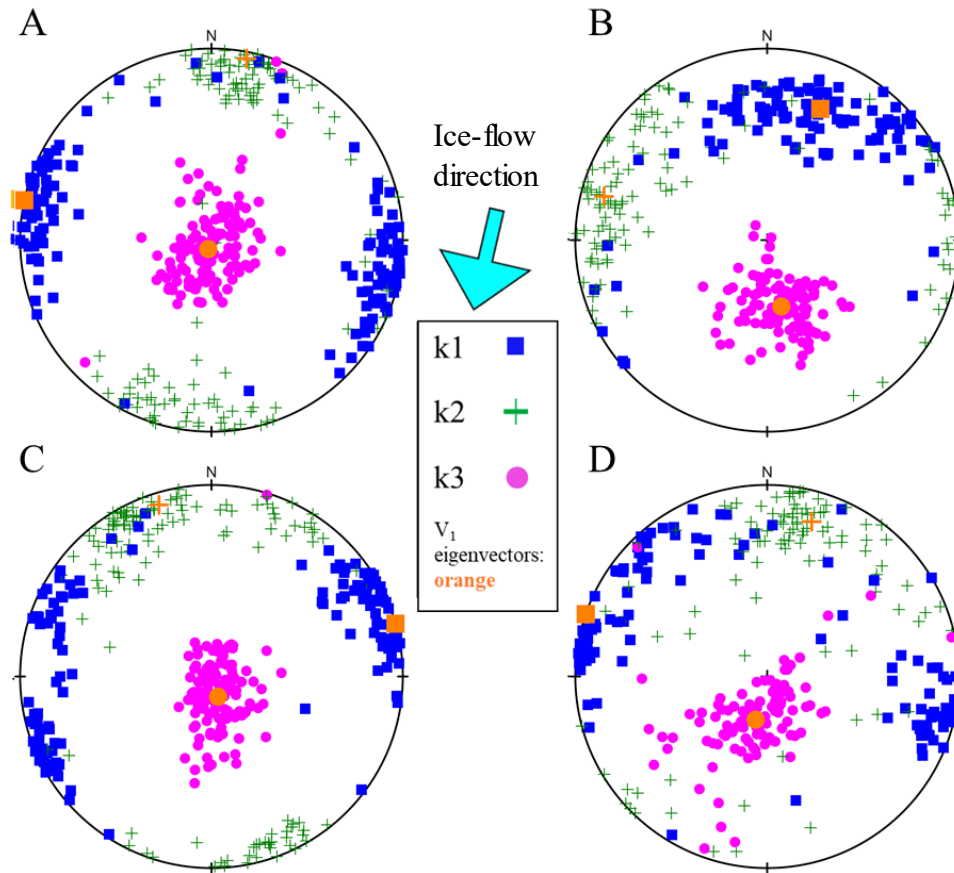
Figure 10. Principal-susceptibility orientations for the six fabrics from the distal end of the Rubjerg Knude thrust complex (Ulstrup section). Large orange symbols show V_1 eigenvectors calculated from the principal-susceptibility distributions.

1090

1091

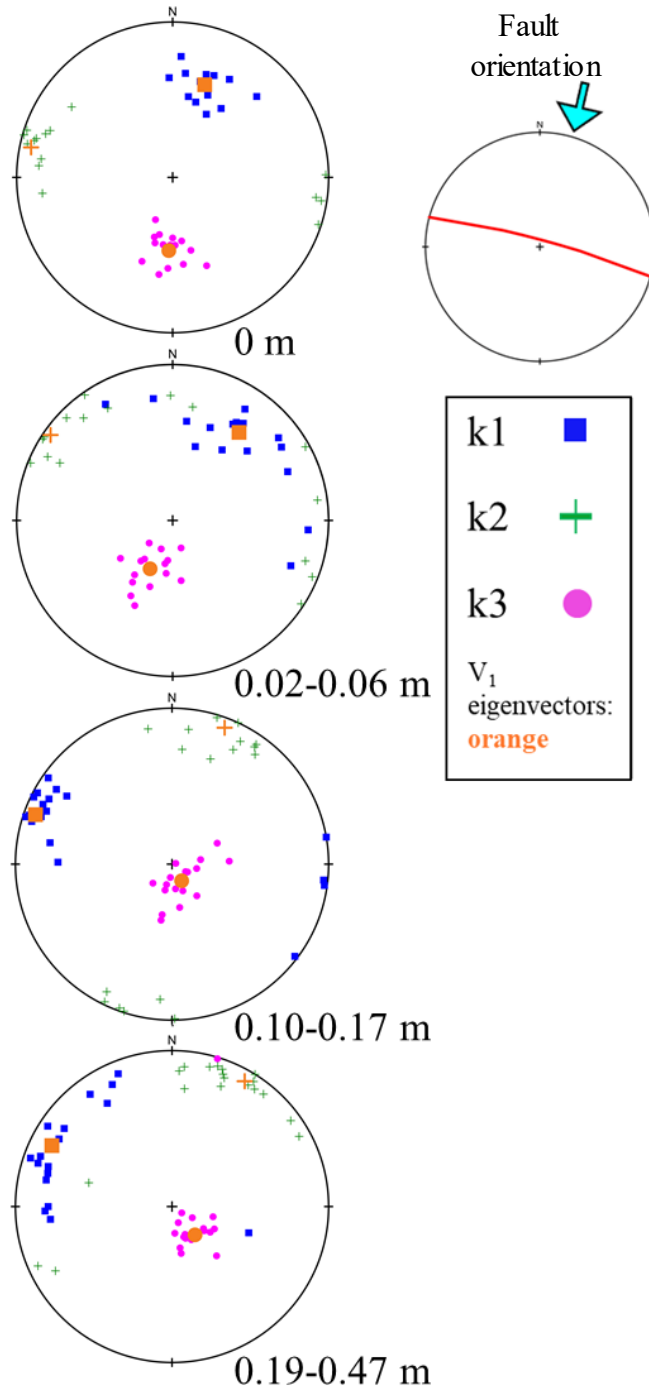
1092

1093



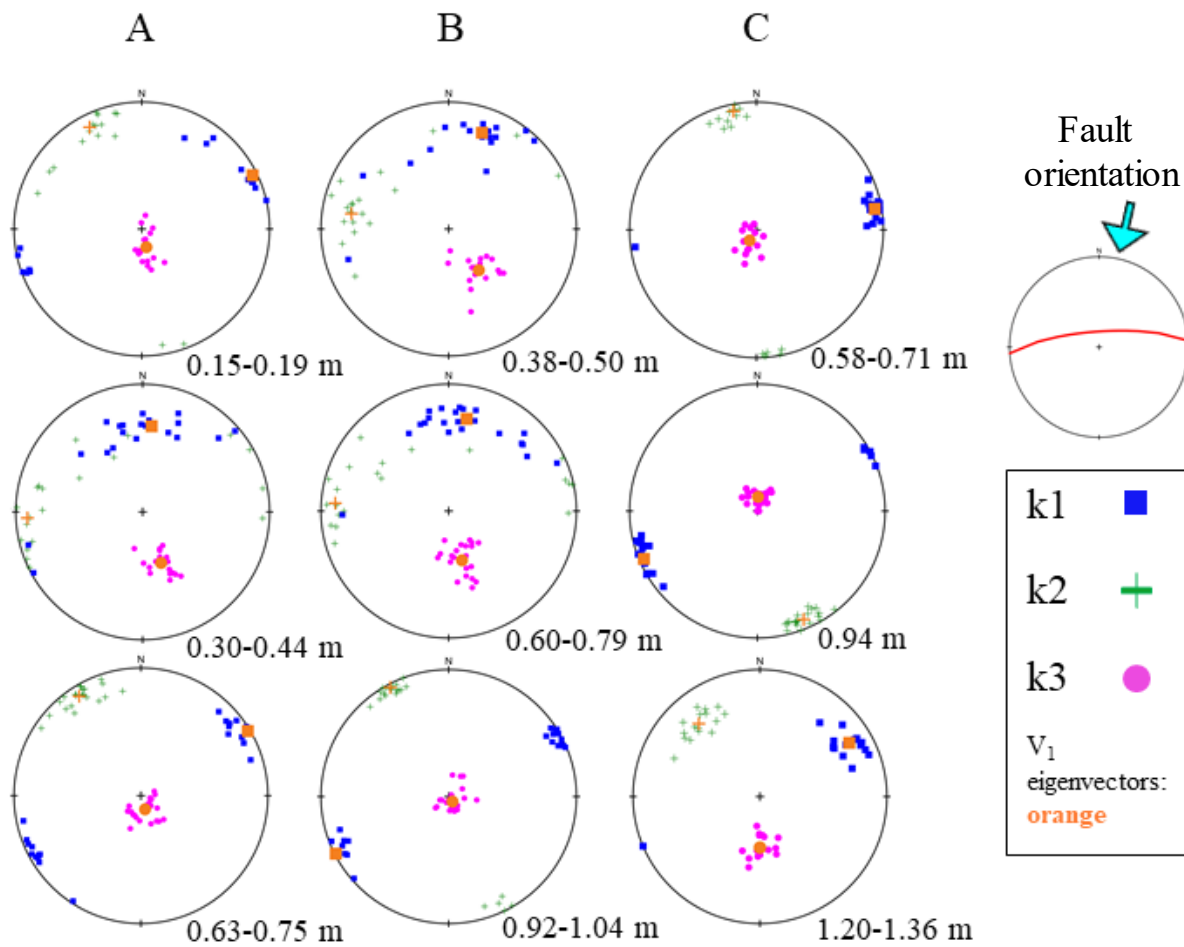
1094
 1095
 1096
 1097
 1098
 1099
 1100
 1101
 1102
 1103
 1104
 1105
 1106
 1107
 1108
 1109
 1110
 1111

Figure 11. Aggregated principal susceptibility orientations at Rubjerg Knude. (A) Principal-susceptibility orientations aggregated for fabrics from the distal end of the thrust complex (Ulstrup section). S_1 values for k_1 , k_2 and k_3 are 0.86, 0.81 and 0.89, respectively. (B) Principal-susceptibility orientations aggregated for fabrics within ~ 0.1 m and ~ 0.7 m of the GR10 and GR05 fault surfaces, respectively, within the Grønne Rende section. S_1 values for k_1 , k_2 and k_3 are 0.78, 0.77 and 0.92, respectively. (C) Principal-susceptibility orientations aggregated for fabrics more than 0.1 m and ~ 0.7 m away from the GR10 and GR05 fault surfaces, respectively. S_1 values for k_1 , k_2 and k_3 are 0.81, 0.80 and 0.92, respectively. (D) Principal-susceptibility orientations aggregated for fabrics from eroded dip-slope surfaces away from faults. S_1 values for k_1 , k_2 and k_3 are 0.76, 0.73 and 0.85, respectively. Large orange symbols show V_1 eigenvectors calculated from the principal-susceptibility distributions.



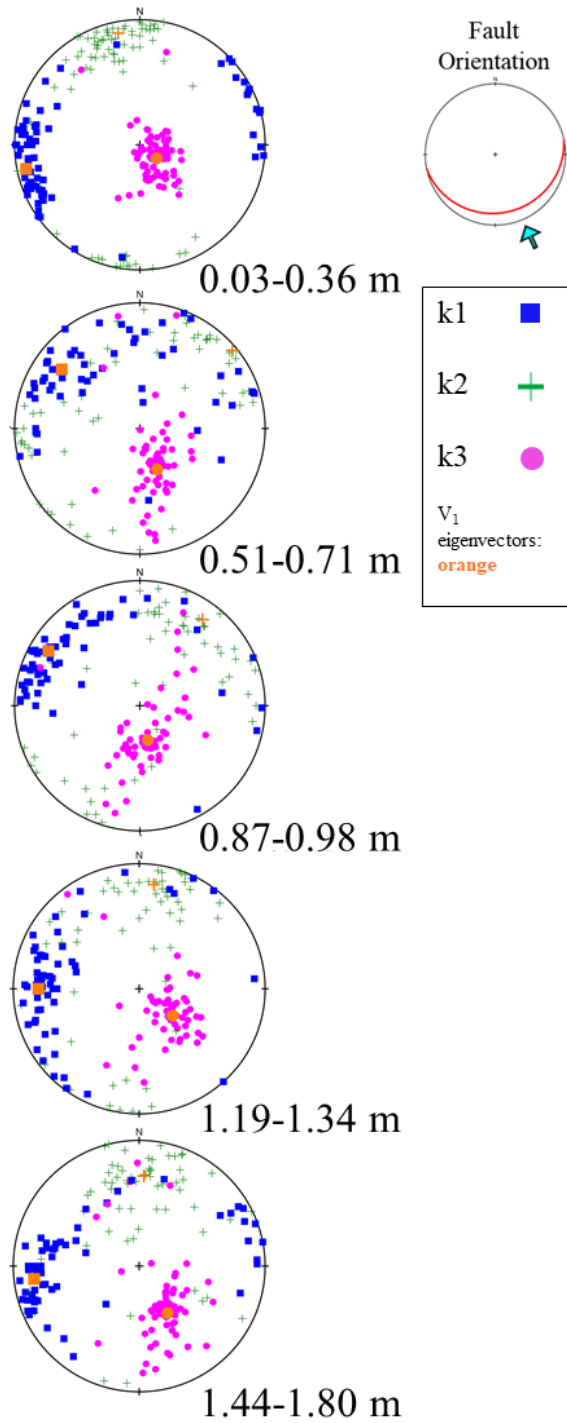
1112
 1113
 1114
 1115
 1116
 1117
 1118
 1119

Figure 12. Four fabrics from thrust sheet GR10 from the Grønne Rende section of Rubjerg Knude. Distances listed are relative to the adjacent fault surface. The fault orientation is shown in a lower-hemisphere stereonet at upper-right, and the cyan arrow shows the ice-advance direction. Large orange symbols show V_1 eigenvectors calculated from the principal-susceptibility distributions.



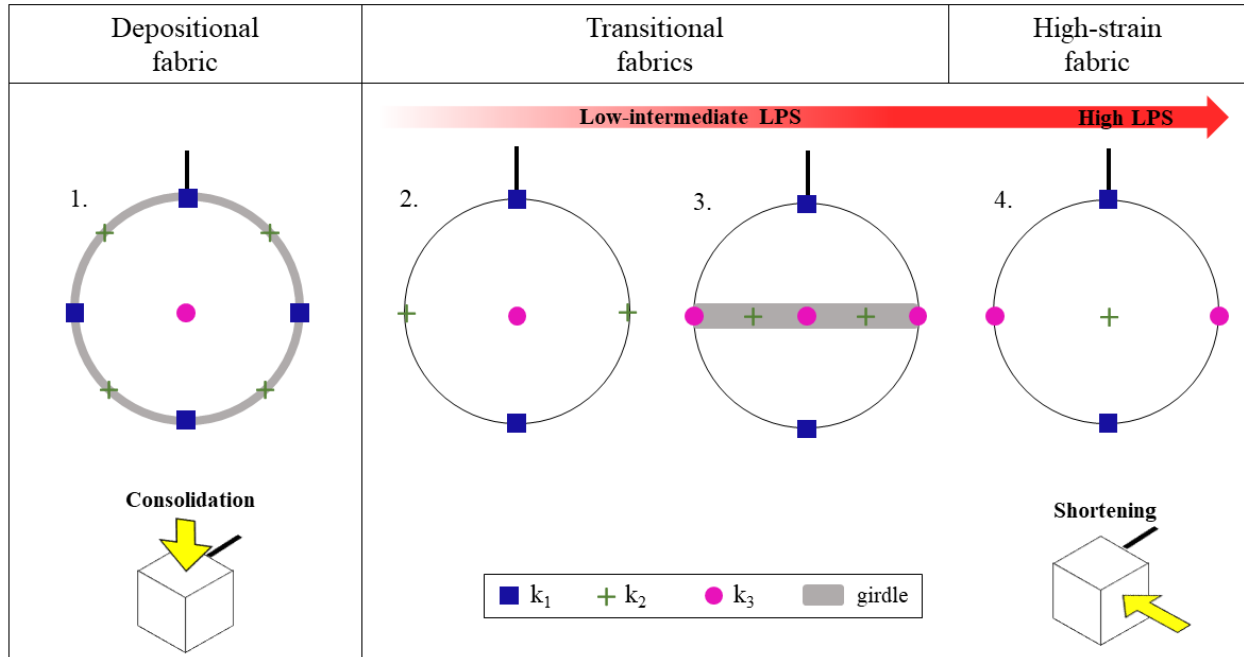
1120
 1121
 1122
 1123
 1124
 1125
 1126
 1127
 1128
 1129
 1130
 1131

Figure 13. Nine fabrics from transects A, B, and C in the thrust sheet GR05 from the Grønne Rende section of Rubjerg Knude (see Fig. 7B for transects). Distances listed are relative to the nearest fault surface. The fault orientation is shown in a lower-hemisphere stereonet at upper-right, and the cyan arrow shows the ice-advance direction. Large orange symbols show V_1 eigenvectors calculated from the principal-susceptibility distributions.



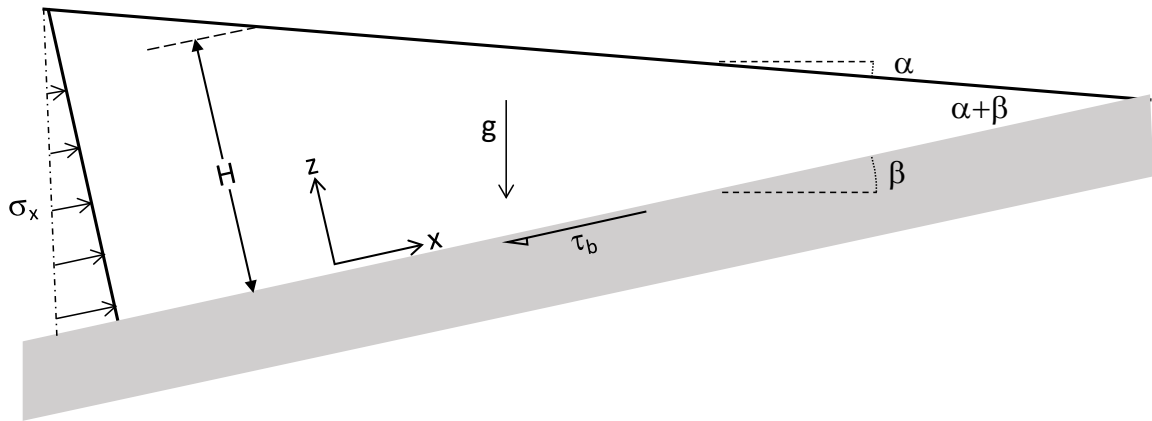
1132
 1133
 1134
 1135
 1136
 1137
 1138

Figure 14. Principal-susceptibility orientations for 17 AMS fabrics collected in the four transects at Møns Klint (see Figure 8), aggregated for five distance ranges from the fault at the chalk-mud boundary. The fault orientation is shown in a lower-hemisphere stereonet at upper-right, and the cyan arrow shows the ice-advance direction. Large orange symbols show V_1 eigenvectors calculated from the principal-susceptibility distributions.



1139
 1140
 1141
 1142
 1143
 1144
 1145
 1146
 1147
 1148
 1149
 1150
 1151
 1152
 1153
 1154
 1155
 1156

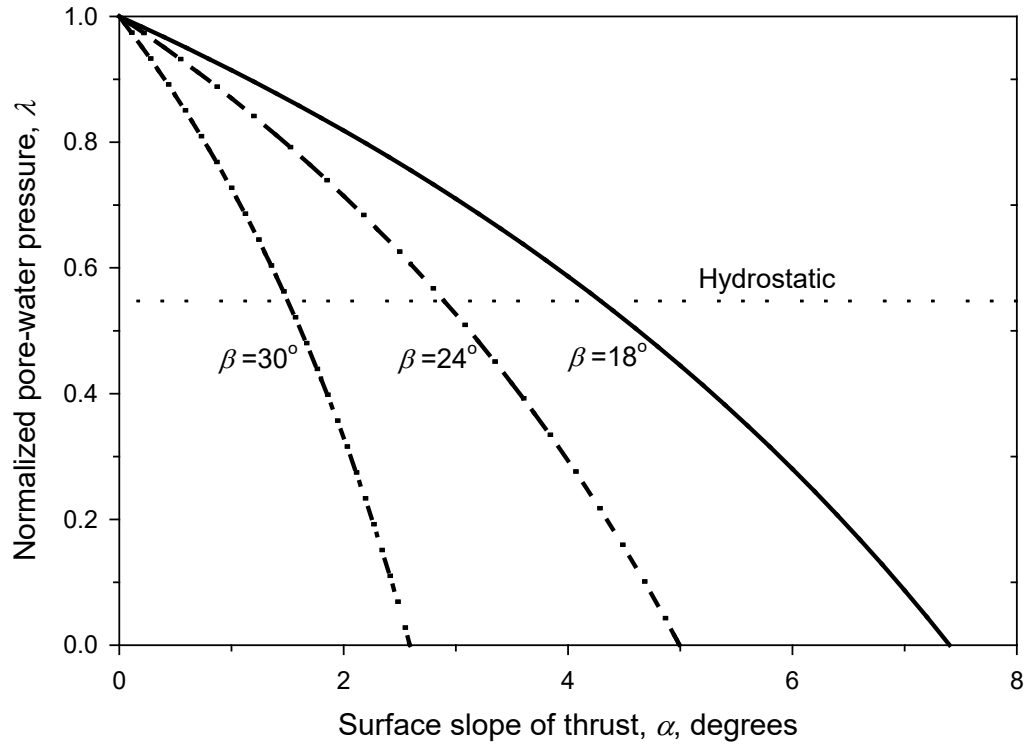
Figure 15. Model for AMS fabric development during deposition/consolidation and layer-parallel shortening (modified from Almqvist and Koyi, 2018).



1157
1158
1159
1160
1161
1162
1163
1164
1165
1166
1167
1168
1169
1170
1171
1172
1173
1174
1175
1176
1177

Figure 16. Schematic diagram of a thrust wedge subject to a push, σ_x (modified from Davis et al., 1983).

1178



1179
1180

Figure 17. Threshold values of pore-pressure ratio, λ , and topographic slope of the thrust wedge, α , above which slip is expected on thrusts without internal deformation of thrust sheets, for different values of thrust dip, β . Zero internal cohesion, $\lambda_b = \lambda$, and $\mu_b = \mu = \tan \varphi$ are assumed, making estimates of λ and α required for slip without internal deformation conservatively large. Also assumed are $\sin \alpha \approx \alpha$ and $\sin \beta \approx \beta$, good to within 5% for the largest angles considered ($\beta = 30^\circ$). The hydrostatic value of $\lambda = p_w / \sigma_z$ is based on a groundwater table at the ground surface, a sediment porosity of 50%, and rock particle density of 2700 kg m^{-3} .

1181
1182
1183
1184
1185
1186
1187
1188
1189
1190
1191
1192
1193
1194
1195
1196
1197
1198
1199

1200 **Appendix Table and Figures**

1201

1202

Table A1. - Parameters derived from hysteresis loop analyses of representative samples from Rubjerg Knude (RK3) and Møns Klint (MUN01)

Parameter	Symbol	Units	<i>Rubjerg Knude</i>	<i>Møns Klint</i>
			RK3	MUN01
Bulk low field magnetic susceptibility	χ_{LF}	m ³ /kg	2.03 x 10 ⁻⁷	1.69 x 10 ⁻⁷
Saturation Magnetization	M _S	Am ² /kg	1.30 x 10 ⁻²	2.54 x 10 ⁻²
Saturation Remanent Magnetization	M _{RS}	Am ² /kg	1.29 x 10 ⁻³	1.37 x 10 ⁻³
Coercivity	$\mu_0 H_C$	mT	11.6	7.16
Coercivity of remanence	$\mu_0 H_{CR}$	mT	46.9	53.3
Squareness ratio	M _{RS} /M _S	--	0.083	0.054
Coercivity ratio	H _{CR} /H _C	--	4.04	7.43
Bulk high field magnetic susceptibility	χ_{HF}	m ³ /kg	7.15 x 10 ⁻⁸	1.93 x 10 ⁻⁸
Magnetite concentration (calculated)	weight percent	%	0.014	0.028

1203

1204

1205

1206

1207

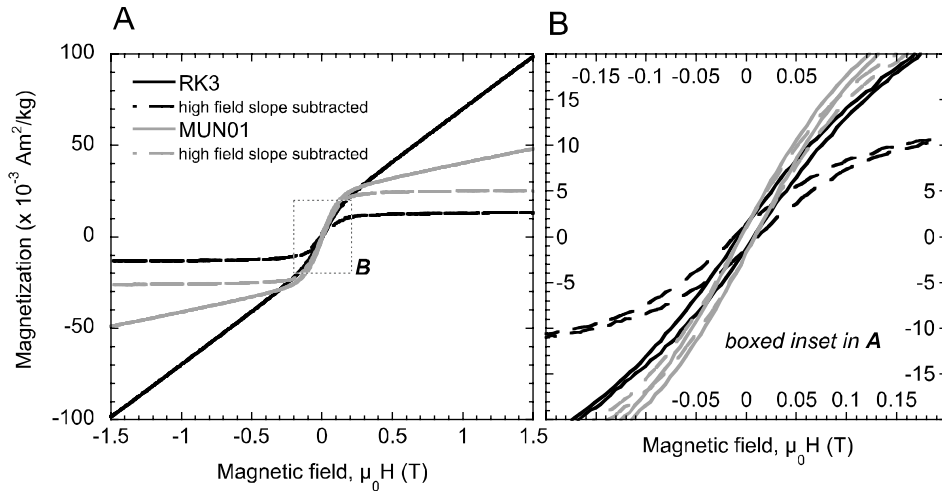
1208

1209

1210

1211

1212



1213

1214

1215 **Figure A1.** (A) Hysteresis loops for samples from Rubjerg Knude (RK3) and Møns Klint
1216 (MUN01) before and after correction. (B) Detail of loops within inset shown in (A).

1217

1218

1219

1220

1221

1222

1223

1224

1225

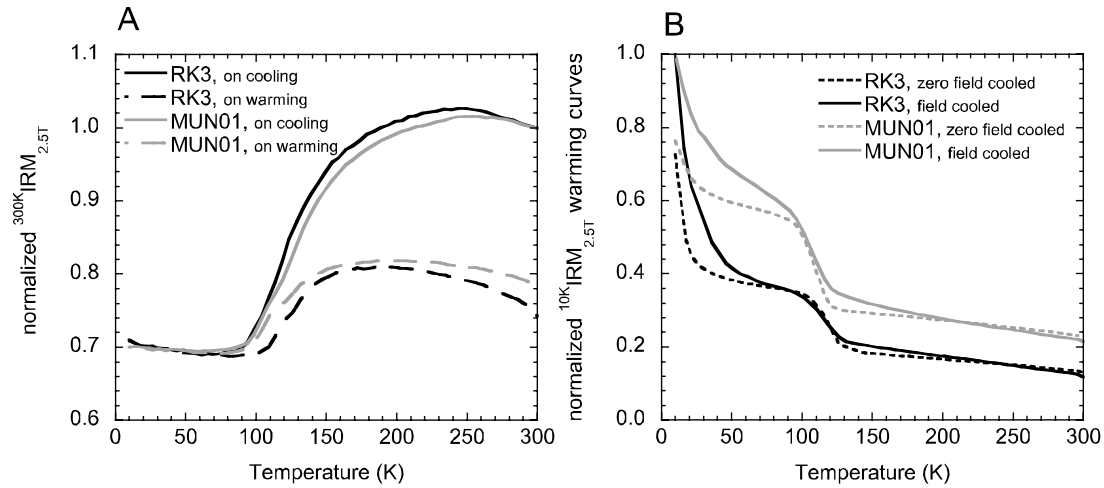
1226

1227

1228

1229

1230



1231

1232

1233 **Figure A2.** Results of low temperature experiments for samples from Rubjerg Knude (RK3) and
1234 Møns Klint (MUN01). (A) 300 K IRM cooling and warming cycles. (B) IRM warming curves.

1235

1236